

Department of Physics and Astronomy
University of Heidelberg

Bachelor Thesis in Physics
submitted by

Luisa Bergmann

born in Ulm-Söflingen (Germany)

2017

Studies of the Gain and Drift Velocity for the ALICE Transition Radiation Detector at the CERN LHC

This Bachelor Thesis has been carried out by Luisa Bergmann at the
Physikalisches Institut of the University of Heidelberg
under the supervision of
Prof. Dr. Johanna Stachel

Abstract

The dependences of the gain and drift velocity of the readout chambers of the ALICE Transition Radiation Detector on pressure and gas mixture were analysed. The HV adjustment parameters for the online pressure correction of the gain and drift velocity were determined and already successfully employed in p–Pb/Pb–p collisions at the end of 2016. The correlation on changes of the gas mixture was investigated and resulted in a rather large decrease for the N₂ dependence of the gain of $(4.2 \pm 1.1) \%$ per 1% N₂ added. The dependence of the gain on the ratio of CO₂ to Xe was found to be less significant than the correlation with N₂. For the drift velocity a similar dependence on the ratio as for the gain was found. By using all corresponding correlations, the data for both the gain and drift velocity were corrected for the dependences on pressure and gas mixture. With these corrections applied, the temporal fluctuations of the gain and drift velocity with respect to the nominal value could be reduced. For the gain, the achieved stability is $(0.92 \pm 0.01) \%$, for the drift velocity $(0.245 \pm 0.002) \%$, with respect to their corresponding nominal values. In the second part of the evaluation, the results were compared to simulations, performed with the Magboltz and Garfield programmes. For the N₂ correlation of the gain, good agreement between simulated and measured data was found within uncertainties. Furthermore, the overall trend of the measured correlations is reproduced by the simulations.

Kurzfassung

In dieser Arbeit wurden die Abhängigkeiten der Verstärkung und Driftgeschwindigkeit der Auslekammern des ALICE Übergangsstrahlendetektors vom Druck und der Gasmischung untersucht. Für die bereits implementierte Anpassung der Hochspannung, bei der die Verstärkung und Driftgeschwindigkeit während der Datennahme bei Druckänderungen korrigiert werden, wurden die Einstellungsparameter ermittelt und bereits in Proton–Blei Kollisionen Ende 2016 erfolgreich eingesetzt. Die bestimmte Abhängigkeit der Verstärkung vom Stickstoffgehalt ergab eine Abnahme der Verstärkung um $(4.2 \pm 1.1) \%$ für jedes zusätzliche Prozent Stickstoff. Die Abhängigkeit der Verstärkung vom Verhältnis des Kohlenstoffdioxids- zum Xenongehalt ist deutlich weniger ausgeprägt als die Abhängigkeit vom Stickstoffgehalt. Für die Driftgeschwindigkeit wurde eine ähnliche Abhängigkeit wie bei der Verstärkung festgestellt. Nachdem die bestimmten Korrelationen zur Korrektur verwendet wurden, konnte eine zeitliche Konstanz der Verstärkung von $(0.92 \pm 0.01) \%$ erreicht werden. Für die Driftgeschwindigkeit ist eine resultierende Stabilität von $(0.245 \pm 0.002) \%$ zu verzeichnen. Im zweiten Teil der Auswertung wurden die Resultate mit Simulationen, durchgeführt mit den Programmen Magboltz und Garfield, verglichen, wobei eine Übereinstimmung der relativen Abhängigkeit der Verstärkung vom Stickstoffgehalt von Daten und Simulationsergebnissen innerhalb der Fehlergrenzen festgestellt wurde. Des Weiteren wird der allgemeine Verlauf der gemessenen Korrelationen durch die Simulationen wiedergegeben.

Contents

1	Introduction	1
1.1	Physics Background	1
1.2	ALICE at the LHC	2
1.3	Outline	4
2	Gaseous Detectors	5
2.1	Interaction of particles with matter	5
2.1.1	Ionisation	5
2.1.2	Transition Radiation	6
2.2	Transport of Electrons and Ions in Gases	6
2.3	Gas Amplification	8
2.4	The Multiwire Proportional Chamber	10
3	The Transition Radiation Detector in ALICE	13
3.1	Physics Requirements	13
3.2	Layout	13
3.3	Gas System	16
3.3.1	Gas Choice	16
3.3.2	Circulation and Pressure Regulation	16
3.3.3	Purification	16
3.4	Electron Identification and Trigger	17
4	Data Analysis	19
4.1	Data Sample	19
4.2	Pressure Correction	21
4.2.1	Gain and Drift Velocity	21
4.2.2	Gas contents	24
4.3	N ₂ Correction	25
4.3.1	Gain	25
4.3.2	Gas mixture	26
4.4	CO ₂ /Xe Correction	27
4.5	Gain and Drift Velocity after all Corrections	29
5	Simulations of Gain and Drift Velocity	31
5.1	Simulating the TRD	32
5.2	Results	34
6	Summary and Outlook	37
A	Data Analysis Plots	39
B	Simulation files	43
	References	50
	Acknowledgements	51

1 Introduction

As it is the general aim of physics to examine and understand the fundamental laws of nature, particle physics takes on this question at the very roots. In the last centuries, our understanding of the smallest structures in the universe has expanded tremendously, owing to continuous technological progress.

1.1 Physics Background

The Standard Model (SM) of particle physics combines our current knowledge of elementary particles and their interactions, excluding gravitation [1]. An overview is given in Fig. 1. All matter is built from the fundamental spin- $1/2$ fermions, the quarks and leptons. The interaction forces between the fermions are transmitted via the gauge bosons (spin-1). The Higgs boson is the only scalar fundamental particle, i.e. it holds a spin of 0. It provides the mechanism through which the gauge bosons of the weak interaction acquire mass in consistency with the requirements of the SM. All fermions partake in the weak interaction, mediated by the charged W bosons or the uncharged Z boson. Only electrically charged fermions feel the electromagnetic force, which is mediated through photons.

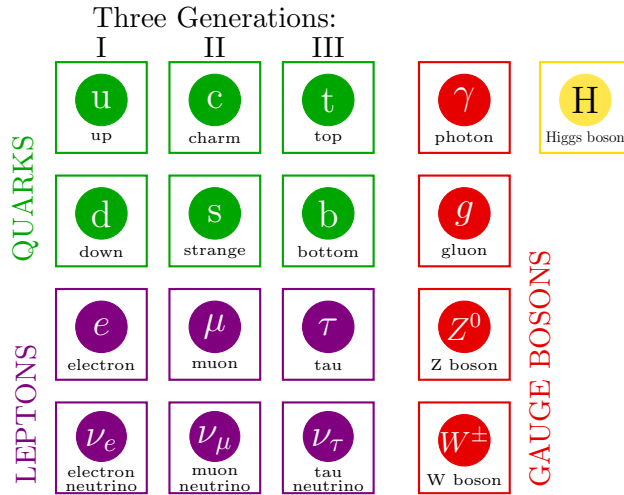


Figure 1: Fundamental particles of the Standard Model (SM) with three generations of fermions, the gauge bosons and the Higgs boson. For every fundamental fermion an anti-particle with opposite charge exists [1].

As quarks are the only fermions to carry colour charge, they are the only ones to participate in the strong interaction. The gauge bosons for this process, gluons, also carry colour charge, which gives rise to a phenomenon called colour confinement [1]. The potential for the strong interaction increases linearly with the distance between the interaction participants [1], which theoretically results in an unlimited amount of energy needed to separate two particles that carry colour charge. In reality, as it is energetically preferable, new quarks are created from the energy of the colour field and are confined in colourless hadrons. Therefore a free particle with non-zero colour charge will never be observed under normal circumstances.

However, a few microseconds after the big bang the temperatures and energy density were high enough to produce a strongly interacting, colour deconfined matter, the quark–gluon plasma (QGP) [2]. Colliding heavy nuclei in high energy particle

collider experiments enables the creation of the QGP. By measuring the properties of particles emerging from the collision — as is done in ALICE at the LHC (Section 1.2) — this state can be analysed. Suitable probes for the study of the QGP are for example heavy-flavour hadrons like the J/ψ meson. Their production contains important information on QGP characteristics, as it is strongly dependent on the medium conditions [2, 3]. As they have a rather short lifetime, J/ψ mesons can only be detected via their decay particles. Due to the fact that leptons do not participate in the strong interaction, the decay to electron–positron or muon–anti-muon pairs is accessible in measurements. For the same reason di-lepton pairs, produced at all stages of the collision, are interesting to analyse [4].

The study of the QGP gives insight to the processes immediately after the big bang and helps to improve our understanding of the strong interaction as well as the formation of the universe as we see it today.

1.2 ALICE at the LHC

At the European Organization for Nuclear Research (CERN), Geneva, Switzerland, scientists from all around the world investigate the fundamental particles and their interactions in various experiments. To access the smallest structures the Large Hadron Collider (LHC [5]) has been built. This ring accelerator with a circumference of 27 km accelerates protons and lead ions and collides them at center-of-mass energies of 14 TeV in pp collisions, 5 TeV in p–Pb collisions and 2.76 TeV in Pb–Pb collisions. At the collision points the detectors of the four major experiments are installed.

A Toroidal LHC ApparatuS (ATLAS [6]) and the Compact-Muon-Solenoid (CMS [7]) experiment are general-purpose detectors. They both operate to survey the predictions of the SM but are also built to access new physics like the search for supersymmetry. Their major success to date is the discovery and confirmation of the Higgs boson in 2012 [8, 9].

The Large Hadron Collider beauty (LHCb [10]) experiment’s aim is to research CP violation in the decays of B mesons (particles containing beauty or anti-beauty quarks). The goal is to explain the existent matter–antimatter asymmetry.

A Large Ion Collider Experiment (ALICE [11]) is the dedicated heavy ion detector at CERN, build to investigate the quark–gluon plasma created in ultra-relativistic heavy ion collisions. The ALICE detector consists of several subsystems (Fig. 2) to discover the whole range of produced particles.

Surrounded by a large solenoid magnet, providing a magnetic field of $B = 0.5$ T along beam direction, the central barrel of ALICE covers the full azimuthal range and a pseudorapidity range of $|\eta| < 0.9$. It contains the Inner Tracking System (ITS), Time Projection Chamber (TPC), Transition Radiation Detector (TRD), Time Of Flight (TOF) detector, High-Momentum Particle IDentification system (HMPID), PHOton Spectrometer (PHOS), ElectroMagnetic Calorimeter (EMCal) and the ALICE COsmic Ray DEtector (ACORDE). Furthermore a muon spectrometer in the pseudorapidity region $-4.0 < \eta < -2.5$ and the forward detectors V0, T0 and ZDC on both sides of the interaction point (IP) for the task of characterising the event are installed.

The ITS is the detector closest to the IP. It consists of six layers of silicon detectors used for low momentum particle identification, primary and secondary vertex recon-

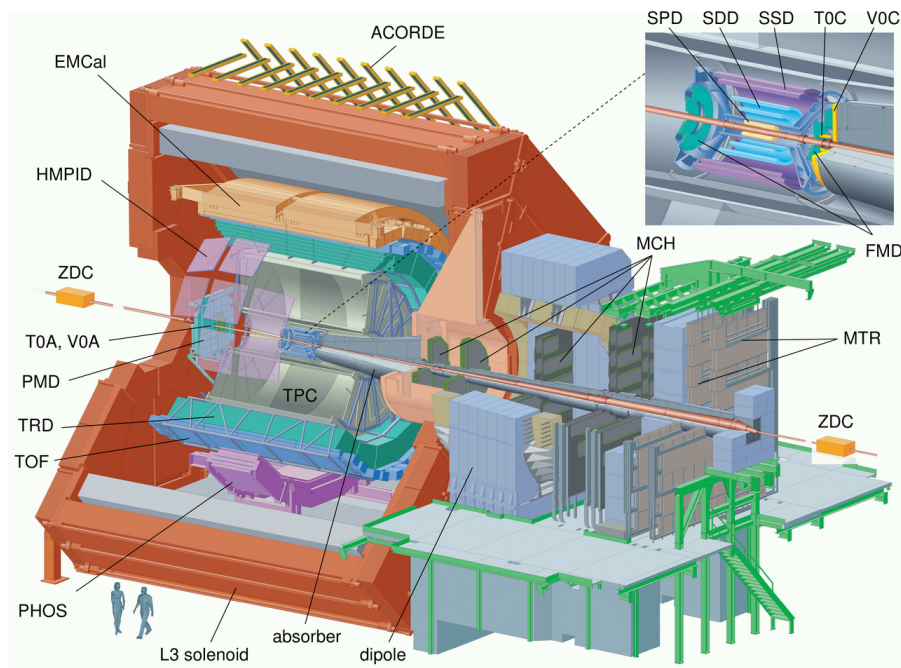


Figure 2: Schematic view of the ALICE detector system with the central barrel detectors, the muon arm and forward detectors on both sides of the IP [12].

struction as well as improving the momentum resolution for reconstructed charged particles.

As the main tracking device, the TPC is the detector with the largest volume. It is mainly used for particle identification (PID, in combination with ITS information) and tracking.

The TRD follows the TPC in the radial direction. It is mainly used for electron identification and triggering. As the TRD is the detector addressed in this thesis, a more detailed description will follow in Section 3.

The TOF detector and the HMPID are used for particle identification at intermediate momenta and above the momentum range accessible through energy-loss or time-of flight measurements, respectively.

The PHOS is built to measure photons to study thermal and dynamical conditions right after the collision, whereas the EMCal focuses on jet quenching and triggers on photons and electrons.

The last detector of the central barrel is ACORDE. It provides a cosmic trigger for alignment and PID studies.

1.3 Outline

This thesis concentrates on the study of the dependence of the gain and drift velocity of the Transition Radiation Detector on pressure and gas mixture. In order to enable a steady and efficient performance of the TRD, both gain and drift velocity are required to be constant in time. Therefore the aim of this thesis is to determine correlation parameters for pressure and gas corrections of both quantities.

In Section 2 a general overview of gaseous detectors is given. In Section 2.1 some interactions of particles with matter that are particularly relevant for the TRD are discussed. Additionally, the expected dependencies of the gain (Section 2.3) and drift velocity (Section 2.2) on the pressure and gas mixture are illustrated.

Next, in Section 3, the design considerations (Section 3.1) and layout (Section 3.2) of the TRD are presented. In Section 3.3 an overview of the gas system is given and Section 3.4 describes the electron identification and trigger of the TRD.

A description of the analysis follows in Section 4, including an explanation of the data set (Section 4.1) and the single steps of the evaluation (subsections 4.2–4.4). Finally, the resulting correlations are compared to Garfield [13] simulations in Section 5.

The results of this thesis are summarised in Section 6. In addition an outlook on further possible studies of the gain and drift velocity is provided.

2 Gaseous Detectors

To detect and identify charged particles produced in high energy collisions detectors are needed. They can be constructed in various forms and with different detection materials, such as gas, semiconductors or scintillating material. Since for this thesis the detector of interest contains gas, only gaseous detectors will be explained in further detail.

2.1 Interaction of particles with matter

Due to the previously described fundamental forces, particles interact with each other when they are within the interaction range of the respective force. Those interactions can be utilised to detect particles.

2.1.1 Ionisation

A charged particle that crosses a gas volume ionizes the gas atoms along its path [1]. The energy transfer occurs due to electromagnetic interactions between the particles, whereas the mean ionisation energy lost by the incident particle (except electrons) can be described by the Bethe-Bloch formula [14]

$$-\left\langle \frac{dE}{dx} \right\rangle = \frac{4\pi N_A r_e^2 m_e c^2 z^2 Z}{\beta^2 A} \left[\frac{1}{2} \ln \frac{2m_e c^2 \beta^2 \gamma^2 T_{max}}{I_e^2} - \beta^2 - \frac{\delta(\beta\gamma)}{2} \right] \quad (1)$$

where $\beta = v/c$ describes the velocity of the charged particle, r_e the classical electron radius, z the atomic number of the incident particle and $I_e \sim 10Z$ eV (for $Z > 20$) the effective ionisation potential of the detector material. Z and A are the atomic number and atomic mass number respectively. T_{max} is the maximum kinetic energy that can be lost by the incident particle in one collision, $\delta(\beta\gamma)$ represents a correction for density effects. The dependence of the mean ionisation energy loss on the particle velocity for various materials can be seen in Fig. 3.

Due to the inverse dependence on the velocity, the ionisation loss is greatest for particles with a low velocity. Particles with $\beta\gamma \approx 3$ are minimally ionizing. Highly energetic particles, that have rather high velocities, are in the relativistic rise of the curve.

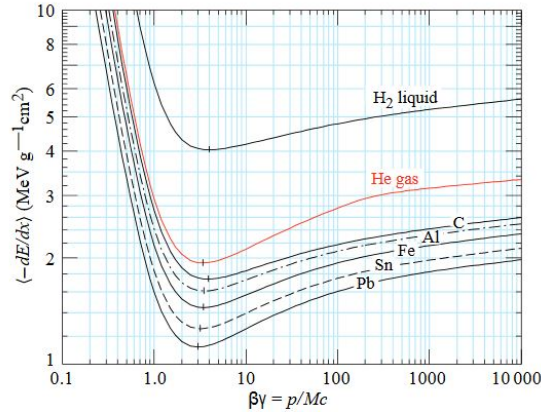


Figure 3: Mean ionisation energy loss as a function of the particle velocity for different materials [14].

2.1.2 Transition Radiation

Furthermore, the occurrence of transition radiation (TR) is of high importance for the TRD. Predicted by Ginzburg and Frank [15], it is produced by a charged particle that traverses two materials with different dielectric constants. At the border between the materials the traversing particle emits electromagnetic radiation, for highly relativistic particles ($\gamma \gtrsim 1000$) in the X-ray domain [16]. The threshold for an efficient detection of TR is at $\beta\gamma \gtrsim 800$ [12].

2.2 Transport of Electrons and Ions in Gases

The general working principle of gaseous detectors involves the creation of free charge carriers, the drift and amplification through the detector and finally the signal generation and read-out.

As the incident particle produces ionisation electrons and ions, those drift along the field lines of an applied electric field. Due to the electrical field strength the particles are accelerated, but lose energy in collisions with the gas atoms. On average a constant *drift velocity* v_{drift} is reached. Since the used gas pressures result in large distances between the collisions (compared to the Compton wavelengths of the ionisation particles) a quantum mechanical treatment of the interactions is unnecessary, i.e. the classical approach can be used.

The drift velocity [17]

$$\vec{v}_{\text{drift}} = \mu \vec{E} \quad (2)$$

in a gas is proportional to the applied electrical field \vec{E} . The mobility μ describes the ability of the charges to move through the gas without losing kinetic energy in collisions. At this point it should be noted that in the central barrel of ALICE a magnetic field of 0.5 T is applied [12]. Technically, this affects the drift velocity as well, cf. for example [18]. However, in xenon mixtures for magnetic fields up to 0.6 T no relevant correlation to the drift velocity was found [4]. The only visible effect is the Lorentz angle, i.e. the ionisation particles do not drift exactly along the electric field lines but at an angle to them. For the evaluations of this thesis this has no relevance.

The goal of this thesis is to achieve a constant drift velocity in the TRD during data taking by determining correlation parameters regarding the gas pressure and mixture and using them for corrections. Therefore some first estimations on what to expect will be described, referring already to some extent to the conditions of the TRD (described in Section 3).

The gases used in modern particle detectors are often argon (Ar), xenon (Xe) or neon (Ne). Those noble gases are characterised particularly by a low reactivity. Due to this property and the usually relatively low pressures, the model of an ideal gas can be employed. For heavy gases like Xe, the approximation becomes inaccurate due to the spatial extensiveness of the atoms. However, this circumstance is only relevant for the handling of the gas and not for the transport properties [19].

As stated before, v_{drift} is dependent on the mobility μ , defined by the Einstein relation [17]

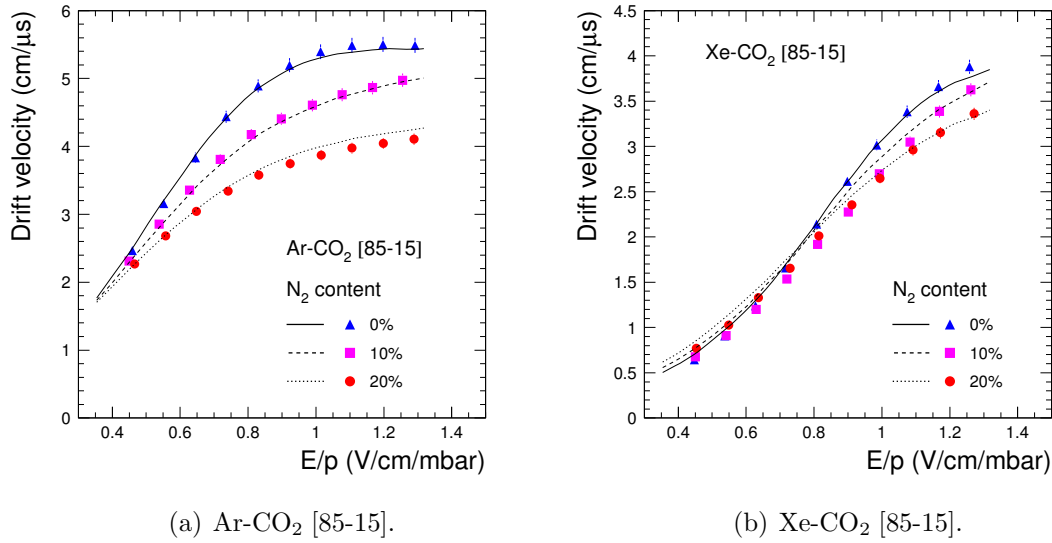


Figure 4: Drift velocity for the ALICE TRD geometry vs. pressure corrected electric field strength for different gas mixtures in comparison with simulations (lines) [20].

$$\mu = De/k_{\text{B}}T \quad (3)$$

with the Boltzman constant k_{B} , gas temperature T , elementary charge e and diffusion constant D .

Using $D \sim \lambda$ [17], the mobility is proportional to the mean free path length λ . As a large number of gas atoms causes more frequent collisions, λ itself is inversely proportional to the particle density in the gas. Hence

$$v_{\text{drift}} \sim \frac{1}{N} = \frac{k_{\text{B}}T}{pV} \quad (4)$$

with the number of particles N , pressure p and volume V of the gas.

In particle detectors the gas volume V is constant, as well as the temperature T , which is regulated to within rather small fluctuations. Consequently, regarding these parameters the drift velocity is mainly dependent on the gas pressure and is expected to decrease with increasing pressure.

Along with the gas properties the gas mixture also has an influence on the drift velocity. In Fig. 4 the dependence of \vec{v}_{drift} on the electric field for two different gas mixtures is depicted. The main constituents of the mixtures are Ar in one case and Xe in the other, both noble gases. To avoid a complete discharge of the gas in the case of large charge deposition during usage in detectors often a quencher gas, e.g. carbon dioxide (CO₂), is mixed in. Due to mechanical imperfections, air from the surrounding areas can enter the detector. For the TRD, the contamination by water and oxygen can be prevented up to a negligible level by integrated filter systems (Section 3.3.3). However, nitrogen (N₂) contamination requires an advanced recovery process [4], which makes it impossible to limit the admixture of this gas. Therefore the N₂ admixture has to be considered in a comprehensive analysis.

As can be seen in Fig. 4, the drift velocity increases with increasing electric field strength. In the Ar mixture an increasing concentration of N₂ results in a decreasing drift velocity. To keep the drift velocity constant a higher drift voltage would be needed with increasing contamination. In comparison the Xe mixture shows a much weaker dependence on the N₂ concentration. For field strengths up to ~800 V/cm the drift velocity is expected to be nearly independent for concentrations ≤20%. In the ALICE TRD an electric field of 700 V/cm is applied and therefore a negligible N₂ dependence expected.

2.3 Gas Amplification

Due to the fact that the particles of the primary ionisation are usually too low in number to create an observable signal, an amplification region follows the drift region in particle detectors. The gain in gas chambers will be described in the following. When the ionisation particles enter the amplification region, the usually high applied electric field accelerates them to energies high enough so they can produce secondary ionisation. Those free electrons are then accelerated again to ionize additional gas atoms and so forth. This multiplication of free charge carriers forms an avalanche towards the field source and can be described by the *first Townsend coefficient* α . The number of electrons N increases with the path length s they travel [18]

$$dN = N\alpha ds \quad (5)$$

α is dependent on the electric field. In detectors an often used concept is the proportional wire, whose field strength increases closer to its surface. Hence, while integrating Eq. 5, one has to consider the path travelled by the particles, i.e. the starting point of the amplification s_{\min} and the radius of the wire, a . Analogously one can calculate in terms of field strengths and integrate from E_{\min} , the field minimal needed to start the avalanche, to $E(a)$, the field at the surface of the wire [18]

$$\text{gain} = \frac{N}{N_0} = \exp \int_{s_{\min}}^a \alpha(s) ds = \exp \int_{E_{\min}}^{E(a)} \frac{\alpha(E)}{dE/ds} dE \quad (6)$$

The change of the electric field along the path of the amplified particle is described by dE/ds . N_0 is the number of primary ionisation electrons, N the final number of electrons after the amplification process has finished. Consequently, the amplification, or gain, of a detector is given by the relative increment in electron number, thus the integral over α .

A. Zastawny [21] showed that

$$\frac{\alpha}{p} = A \exp\left(\frac{-Bp}{E}\right) \quad (7)$$

provides a very good description of the measured data. E and p are the applied electric field and gas pressure, respectively. A and B are gas dependent parameters that have to be measured for every gas mixture. An illustration of Eq. 7 with A and B taken from [21] for a gas mixture of Xe-CO₂ [95-5] and an electric field of

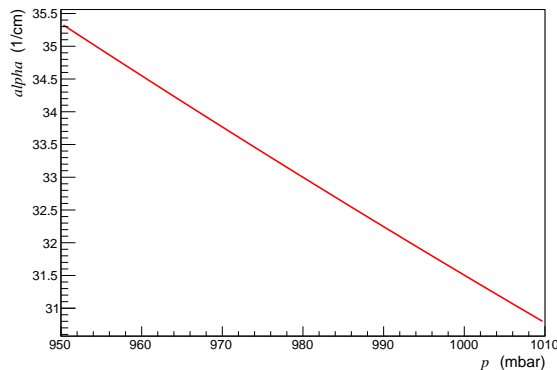


Figure 5: Townsend coefficient α vs pressure for the gas mixture Xe-CO₂ [95-5] with parameters for Eq. 7 taken from [21].

40 kV/cm — the average present in the amplification region of the ALICE TRD, cf. Section 3.2 — for pressures around atmospheric pressure is shown in Fig. 5. In the pressure range relevant for the TRD the Townsend coefficient decreases with increasing pressure. Therefore an inverse proportionality of gain and pressure is expected.

The gas parameters in Eq. 7 and the results in [21] reveal a very strong dependence of α on the gas mixture. Analogous to the previous section, the correlation of the gain and the electric field for two different nominal gas mixtures with increasing N₂ contamination is shown in Fig. 6. However, other than in Section 2.2, the data sets show a clear behaviour of the gain for both noble gases. With increasing N₂ content the gas gain decreases noticeably. In the Xe based mixture, for example, an adjustment of 50 V for every 10% of added N₂ is needed to keep the gain constant.

Shown also, via dashed and continuous lines, are simulations with the Garfield package (explained in further detail in Section 5) of the expected gain for the given gas mixtures and field strengths. As can be seen, the dashed lines underestimate the gain for both gas mixtures tremendously. The continuous lines yield a far better description, as in this case the increasing influence of the Penning effect (Eq. 8 [18]) on the gain was included. This effect considers the different excitation and secondary ionisation processes in gases composed of more than one component. Depending on the different energy levels of the gas constituents, one component C, if in an excited state C*, may be able to ionize the other one (D) through energy transfer in collisions.



This occurs if the excited state of C has a higher energy than the ionisation energy of D. Hence, in a Penning mixture the gain is higher than in a gas with simple avalanche multiplication due to the additionally ionized gas atoms.

In most cases, D is the quencher gas as it is for the mixture Ar-CO₂. The average excitation energy of Ar is 14.0 eV and therefore higher than the ionisation potential of CO₂ (13.773 eV) [20]. So in collisions, CO₂ can be ionised by Ar.

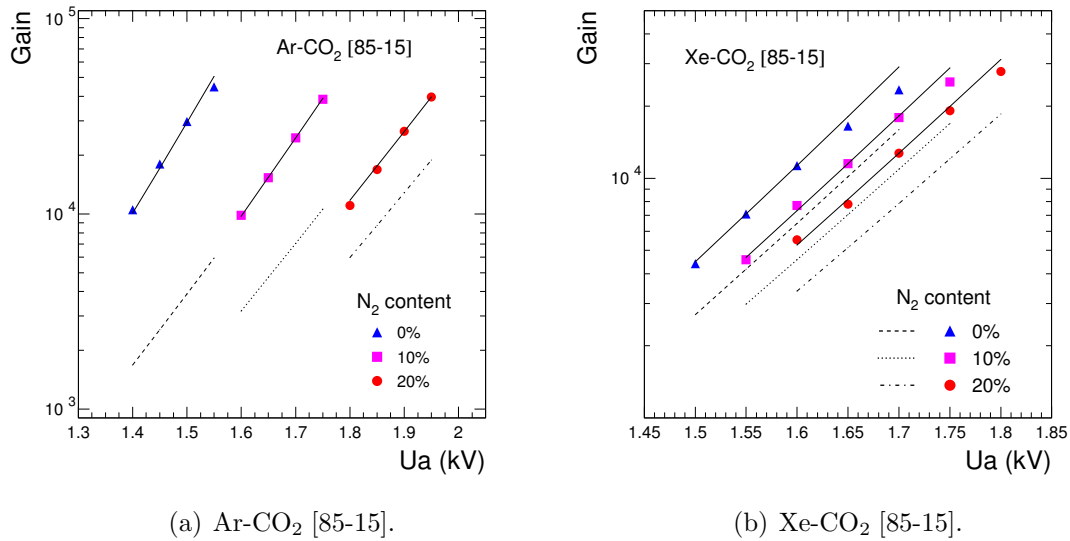


Figure 6: Gain for the ALICE TRD geometry as a function of the anode voltage for different gas mixtures in comparison with simulations performed with (continuous lines) and without (dashed lines) the Penning effect [20].

2.4 The Multiwire Proportional Chamber

In particle detectors, the previously described processes are applied to obtain particle identification and position determination via the measurement of ionisation energy loss and spatial resolution of the induced signal, respectively. The most used concept, in various extensions, is the Multiwire Proportional Chamber (MWPC) which provides particle identification and 2D position determination [17].

Basically, a MWPC consists of numerous anode wires, equally spaced, between two cathode plates. The volume is filled with gas. When the gas is ionized by a traversing particle, the primary electrons are amplified, as described in section 2.3, in the vicinity of the closest anode wire. The avalanche electrons induce a short signal on the anodes. The ions produced in the avalanche drift away from the anode wires towards the other electrodes and induce a signal due to their movement on both the anode wires and the cathode plates [18]. As this drift is, due to the rather large mass of the ions, very slow — 1000-fold slower than the electrons[18] — the signal is long enough in duration to be read out. As the name indicates, the signal is proportional to the energy lost by the original particle and can therefore be used for particle identification.

To obtain information about the particle position, the spatial position of the wires can be utilised. When a particle crosses the anode plane at an angle (Fig. 7), the ionisation particles will induce a signal on more than one wire. This holds 1-dimensional position information. For a second dimension, the cathode plates can be involved in the analysis by segmenting them and placing the stripes perpendicular to the anode wires. The 2D position is then obtained by combining both signals. Another possibility is the installation of several MWPCs on top of each other. By orienting the anode wires at different angles, the 2D position can be obtained by combining the information of all layers.

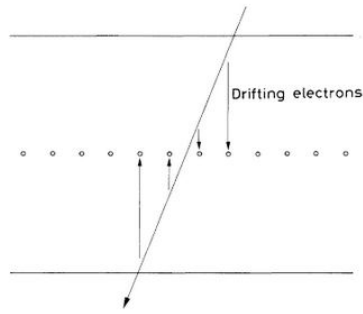


Figure 7: Track clusters caused by particles arriving at an angle to the anode plane [17].

The TRD, described in the next section, consists of such MWPCs and additional drift volumes. As the drift velocity is known a priori, the 3-dimensional track of the traversing particle can be reconstructed with the 2D MWPC information and the calculation of the radial position from the ionisation particles' drift times through this drift volume.

3 The Transition Radiation Detector in ALICE

In the following, the design considerations and the construction of the TRD are described. Moreover, the gas choice as well as the topic of this thesis are motivated, the latter by describing the electron trigger.

3.1 Physics Requirements

As mentioned in Section 1.1, electrons are some of the most interesting probes for the study of the QGP and therefore very good electron identification is crucial. In the TPC, the main PID device in ALICE, the identification above a momentum of 3 GeV/c becomes less efficient [4], as the spectra for the mean specific ionisation energy loss of electrons and pions then start to overlap. Depending on the cuts applied to the data to distinguish both particles, the discrimination works for momenta up to 8 GeV/c, but at the expense of accuracy and statistics [22].

The TRD [4, 12] was designed to provide the required electron identification capabilities. The TRD uses the measurement of both specific energy loss and TR for the identification. As stated in Section 2.1.2, the yield from TR only becomes detectable for $\beta\gamma \gtrsim 800$. At a momentum of $p = 1$ GeV/c, the factor is above this threshold for electrons (as $p = m\beta\gamma$) but not for pions, due to their much larger mass¹. For pions to be able to produce TR, a momentum of at least 112 GeV/c would be needed. As this by far exceeds the detection range of the TRD, the evaluation of mean energy loss in combination with TR yields a very efficient discrimination of electrons and pions.

Furthermore, the TRD provides triggering capabilities for jets at high transverse momentum and electrons for measurements in pp and p–Pb collisions. Probes containing electrons are very rare in these measurements and therefore need to be triggered to acquire sufficient statistics.

By providing both an efficient electron identification and trigger, the TRD clearly makes a considerable contribution to the physics aims of ALICE.

3.2 Layout

The TRD consists of 18 supermodules. They are mounted in the ALICE space frame following the TPC in the radial direction. Every supermodule is built in the same way and forms an autonomous unit, in which 30 single chambers per supermodule are arranged in 5 stacks in the beam direction z and 6 layers in the radial direction (Fig. 8). Consequently the whole TRD provides space for 540 readout chambers that are all constructed in the same way. As it is necessary to place as little amount of material as possible in front of the PHOS only 522 chambers were installed by omitting the middle stacks of the supermodules 13–15 [12]. The expanse of a single chamber ranges from 0.90 m \times 1.06 m to 1.13 m \times 1.43 m [12].

As the special feature of the TRD is the evaluation of transition radiation (Section 2.1.2), a crucial element for the chambers is the radiator. Since transition radiation is electromagnetic, the number of photons emitted at one boundary is on the order of the fine structure constant $\alpha = 1/137$ [16]. So for sufficient photon production usually a large number of boundaries is needed. The most efficient radiator available — a few 100 layers of polypropylene foil — is not applicable in

¹ $m_e \approx 511$ keV/c², $m_\pi \approx 140$ MeV/c² [14]

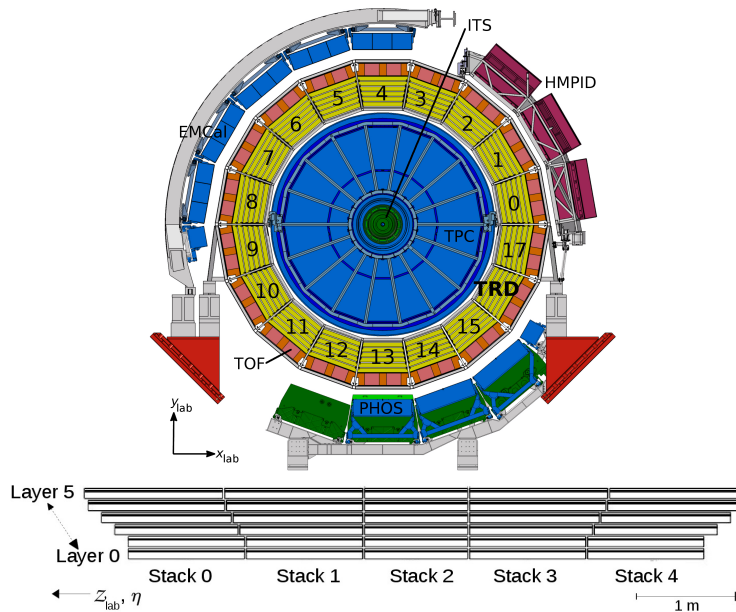


Figure 8: General cross section of ALICE with detailed TRD position and a schematic overview of the supermodule structure [12].

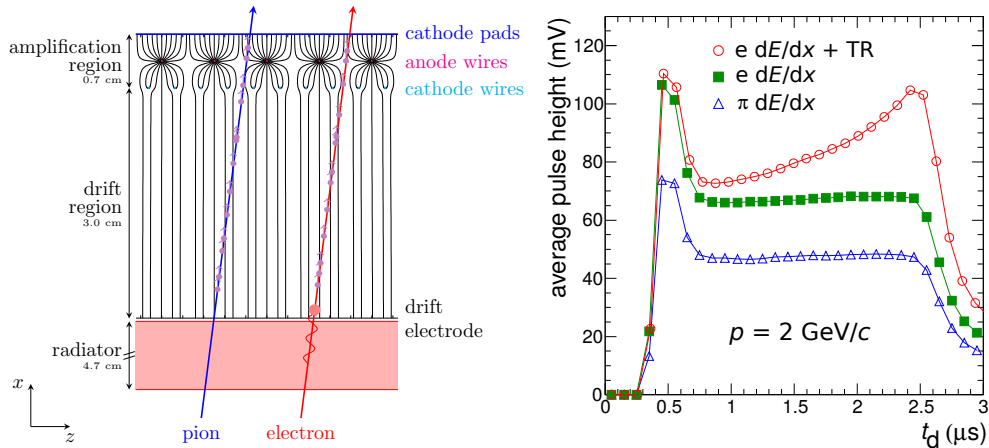


Figure 9: Schematic cross section of a TRD readout chamber and the signal induced on the pads vs. time [12].

the case of the ALICE TRD, as the heavy support needed to carry the weight of the foils conflicts with the requirement of minimizing the amount of material in front of the following detectors [4]. Instead a combination of fibre mats and foam was used, which produces enough photons for an efficient electron identification — about one photon in the X-ray spectrum per electron — and has the additional advantage of supporting the mechanical stability of the TRD. In total, the radiator part has a length of 4.8 cm. Following the radiator, the readout chambers consist of a MWPC preceded by a drift region, filled with Xe and CO₂ at a nominal mixture of [85-15]. Combining all used materials, the TRD has an average radiation length of $\langle X/X_0 \rangle = 24.7\%$ [12]. The choice of gas is motivated in Section 3.3.1. In Fig. 9 a schematic cross section of a readout chamber as well as the signal induced on the cathode pads as a function of time is shown.

On the radiator, an aluminium coated mylar foil is glued, forming a uniform drift field of 700 V/cm [12] over the length of 3 cm confined by a voltage divider chain of

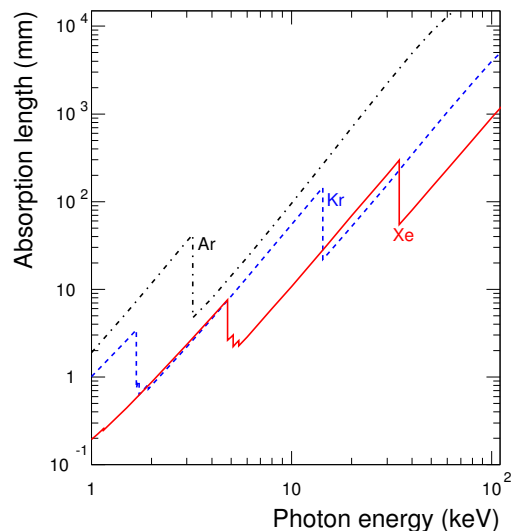


Figure 10: Absorption length as a function of photon energy in different noble gases [12].

cathode wires. The nominal drift voltage of -2.15 kV [12] is adjusted individually for every chamber to align the drift velocities. In this field, the primary ionisation ions drift towards the drift electrode (negative x -direction in Fig. 9), while the ionisation electrons drift towards the anode wires at the end of the chamber with a nominal drift velocity of 1.56 cm/ μ s [12].

After passing the drift volume the ionisation electrons enter the amplification region that has a total depth of 7 mm. At the half way point the anode wire plane is installed. As described in Section 2.3, the electrons are accelerated towards the wires which are set to a nominal anode voltage of about 1.52 kV [12], as well adjusted individually for every chamber, and form an avalanche with a gain of ~ 3200 [12]. The cathode wires at the end of the drift volume, that are almost completely permeable for the electrons from the drift region, build a border for the ions created in the avalanche [4]. Those induce a signal with the shape shown in Fig. 9 as described in Section 2.4. The average pulse height is read out as a function of time in 30 time bins [12]. The peak at early times corresponds to the primary ionisation released near the anode wires. Particles on both sides of the wires are amplified and therefore generate an increased signal. Afterwards only ionisation electrons from the drift region enter the amplification region, which corresponds to the constant part of the signal. When all ionisation particles have reached the wires, the signal decreases, with the tails of the distribution being caused by the slow motion of the ions. As can be seen in Fig. 10, the absorption length for photons in the X-ray range is a few cm in Xe. Therefore, TR is most likely to be absorbed at the beginning of the readout chamber and correspondingly more charge is deposited there in the case of an electron passing through the detector. Due to that fact the induced signal of electrons increases in later time bins.

Spatial localisation can be achieved by evaluating the signal from the same (particle) track induced across several pads and the measurement of the drift time (Section 2.4).

3.3 Gas System

As already described, gas is the main detection material in the TRD and therefore an important part of the detector. The dedication and construction of the TRD define some conditions for both gas choice and gas handling, as described in the following.

3.3.1 Gas Choice

As mentioned in the previous section, the chosen chamber gas for the TRD is a mixture of Xe and CO₂ in proportions of 85 % and 15 %, respectively. There are several factors that justify this choice.

On one hand the TRD requires efficient X-ray absorption. The photoabsorption probability increases with atomic number [4], therefore low mass gases can be excluded a priori. In Fig. 10 the absorption lengths for different noble gases with a relatively high Z are depicted as a function of the photon energy. The energy of a TR photon is typically on the order of 10 keV, for which an absorption length of 1 cm in Xe is obtained. This is much shorter than the absorption length for the other diagrammed gases with lower atomic number. In addition it can be noted that in the chosen gas mixture diffusion is minimized to a level negligible compared to position resolution.

To limit the discharging of the gas in the case of high energy deposition, a quencher gas needs to be added to the mixture. The main advantage of CO₂ is its non-flammability which significantly contributes to the safety of the whole system. Furthermore it is a rather inexpensive gas, in contrast to Xe. The high cost of Xe requires the circulation to be a closed loop through the detector. In addition the density of Xe (5.76 kg/m³ at ambient conditions) leads to a hydrostatic pressure of 2.8 mbar over the height of 7 m of the detector, so a balancing pressure regulation is needed. Both are described briefly in the following subsections.

3.3.2 Circulation and Pressure Regulation

Before the gas is inserted into the detector, it is mixed to the desired ratio by a mixing unit outside the detector system. Subsequently it is circulated through the detector and a purification system via a pump. To ensure mechanical stability the working pressure of the TRD is limited to 1 mbar which is clearly lower than the hydrostatic pressure of 2.8 mbar. Accordingly the circulation has to be done individually with adjusted pressure regulation for each supermodule.

The equality of the overpressure in all sections is achieved by leading the gas through thin (4 mm inner diameter over a length of 100 m) pipelines of equal length in the TRD modules. Thus, the pressure drop over these lines is much larger than the hydrostatic pressure over the detector and an even flow at equal pressure is ensured [4].

3.3.3 Purification

Accounted for by the fact that the volume-to-surface ratio is quite small and the circulation system adds to this, the detector system in total offers a large contact surface for contamination of the gas by air. Hence, filter systems need to be installed to guarantee consistent data taking.

Gas	Freezing point	Boiling Point
N ₂	-209.86 °C	-195.8 °C
Xe	-111.9 °C	-108.1 °C
CO ₂	-78.4 °C (subl.)	

Table 1: Freezing and boiling points of N₂, Xe and CO₂ [4].

An integrated purifier, being two cartridges of activated copper, purges the gas mixture of O₂ and H₂O. The oxygen is removed by oxidation, the water by absorption. However, the N₂ contamination is not taken into account in this purification. For the separation of Xe and N₂ an outlying recovery station is used. It employs the different freezing points of the gases (see Tab. 1) to recycle the Xe devoid of N₂. The gas mixture is placed in a cryogenic recovery unit and cooled down by liquid N₂. Due to the different freezing points, Xe and CO₂ solidify, while N₂ remains in gaseous form. When the N₂ is completely pumped out, the remaining gas is re-heated and can be re-used in the detector. This process is adequate efficient and results only in little loss of Xe or remaining N₂. However, as it takes a rather long time for this process to be completed, it can only be done during a longer stop, e.g. on EYETS every one or two years. In the meantime, the N₂ content increases continuously and affects the detector properties as described in Sections 2.2 and 2.3.

3.4 Electron Identification and Trigger

As explained in Section 3.2, electrons are expected to deposit more charge in the detector than pions, due to a higher specific ionisation energy loss and TR production. This can be used to identify the former.

The electron identification is done by calculating the Likelihood that a signal measured from a charged particle traversing the detector was created by an electron [12, 23]. The Likelihood of the whole track is calculated by combining the probabilities of the single tracklets of all layers. A tracklet is the track segment reconstructed in a single readout chamber. The probability of the tracklet to be produced by an electron is determined via the measurement of the deposited charge of this tracklet and the comparison with Look-Up Tables (LUT) that are stored in the electronics of each supermodule. These LUTs contain the probability that a certain charge deposit was created by an electron. The tables are generated by comparing the total charge distribution of electrons to those of other particle species. In Fig. 11 the distribution for electrons and pions for a single readout chamber, normalized to the tracklet length, is shown. It can be seen that the maximum of the electron distribution is shifted to larger values in comparison to the pion distribution as the specific ionisation energy loss and TR yield increase the signal. Accordingly, the probability that a charge was deposited by an electron is high when the measured signal is similar to this maximum. Moreover, the probability is low for lower measured signals, as the maximum of the pion distribution is located there. At even higher values of the measured signal, the probability decreases again as well, as the charge deposits of electrons and pions are similar there. A schematic Look-Up Table is shown in Fig. 12. The electron identification can be further improved by considering the temporal dependence of the signal height [12]. One example is the sectioning of the signal in time bins, accounting for the expected increase for an

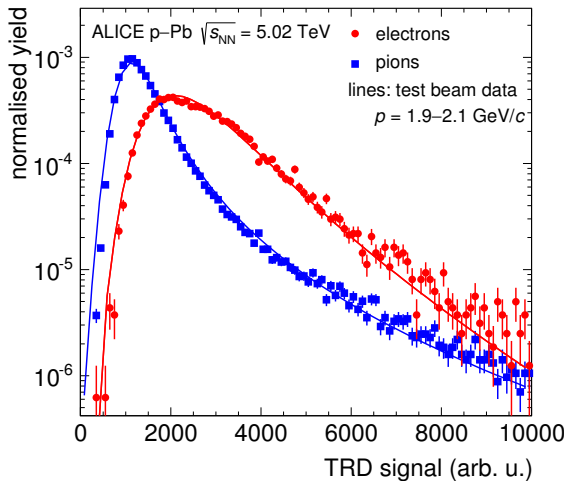


Figure 11: Total integrated charge for electrons and pions in a readout chamber, normalized to tracklet length [12].

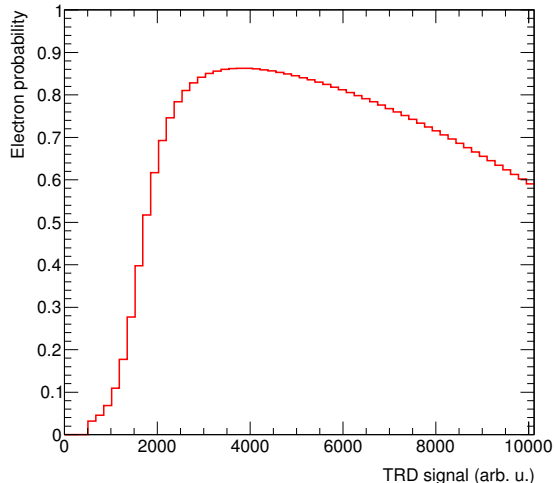


Figure 12: Schematic Look-Up Table [24].

electron signal at large drift times that occurs due to the early absorption of the TR photon (cf. Section 3.2).

The results from the electron identification can be further employed for triggering [12, 23]. As mentioned in Section 3.1, probes with electrons are rare, especially in pp or p-Pb collisions, and therefore need to be triggered. The ALICE trigger system has several stages [11]. The Level-0 (L0) and Level-1 (L1) trigger are sent $1.2\ \mu\text{s}$ and $6.5\ \mu\text{s}$ after the interaction, respectively, preparing the readout detectors for recording of the selected events. After acceptance of the Level-2 (L2) trigger — sent after $88\ \mu\text{s}$ — the recorded data is stored by the Data Acquisition (DAQ). All trigger decisions are processed and distributed by the Central Trigger Processor (CTP). The TRD provides input for the L1 trigger for high- p_T electrons, but also e.g. for jets.

The performance of the detector, concerning PID and triggering capability, is obviously strongly dependent on the stability of gain and, to a certain extent, drift velocity. The LUT, which converts the measured charge deposits into electron likelihoods, was generated for a certain nominal gain [23]. A deviation from this gain will shift the measured charge deposit and thereby the assigned probability. The stability of the drift velocity contributes to the correct online tracklet reconstruction. For efficient operation, both gain and drift velocity are required to be constant in time. As discussed in Section 2, some external parameters, like changes of the pressure and gas composition, impair the stability and therefore an online correction for the gain and drift velocity is needed. In the following section, the determination of the required correction parameters is described and discussed.

4 Data Analysis

As explained in the previous section the stability of the gain and drift velocity, especially of the former quantity, is of high importance for the TRD performance. In this chapter the dependences of the gain and drift velocity on pressure and gas mixture are determined. The criteria, which parameters the correlations were determined for, are orientated on their degree of influence on the gain and drift velocity (Sections 2.2 and 2.3), as well as the amount on which they change over time. The dependence on the temperature was assumed to be negligible, as it is very well regulated, for the chosen data set to a maximum range of 0.5 °C. The contents of O₂ and H₂O are kept at a constant and low level by the previously described purifiers (Section 3.3.3). Therefore the dependence of the gain and drift velocity on those parameters is considerably low and thus neglected as well. For the remaining parameters, the fluctuating pressure has the highest influence on the gain and drift velocity. To be able to respond to pressure changes during data taking, an online correction method was already implemented. In analyses previous to this thesis, updated correction parameters for the gas mixture of Run 2 were determined and compared to the recent results from this thesis. After analysing the pressure dependence of the gain and drift velocity, their dependence on the gas mixture was investigated. As explained in Section 3.3.3, the N₂ contamination can only be removed infrequently and is therefore covered in the following analysis. The third dependence to be analysed in the following is the one on the ratio of CO₂ and Xe. The influence of a change of this quantity is a priori not known, but since the voltage settings are tuned to optimise both the gain and drift velocity to the required values for a specific nominal mixture, this dependence is certainly an interesting one to be investigated.

4.1 Data Sample

For the analysis of the dependences the most recently produced data, i.e. recorded in 2016, was used. The measurements of the gain and drift velocity are accessed via the Offline Calibration Data Base (OCDB), where all sensor data is stored for calibration and reconstruction. The data used in this thesis passed `cpass0`, the reconstruction pass that prepares the calibration in `cpass1` [12]. Pressure and gas mixture are measured independently by a pressure sensor and a gas chromatograph, respectively. The original intention to use all data of the year 2016 could not be accomplished, as different adjustments during this year resulted in incomparableness for both the gain and the gas mixture.

In June 2016 the gas chromatograph was re-calibrated. This introduced as an artefact an additional pressure dependence of the single gas contents that needs to be corrected for. As a consequence, the gas corrections of the gain and drift velocity from data sets both before and after the re-calibration is not possible due to the different scaling of the gas. Furthermore, the high voltage settings have been adjusted several times in the time span from the end of August to midst of September as the increasing N₂ contamination in the TRD caused a decrease of the gain by 10% in the time span from midst of April to the end of August. Accordingly, with new voltage settings, the gain increased again, making the use of data from before and after the HV adjustments impossible.

Eventually - to guarantee consistence - only measurement results from runs were

used, that took place after the completion of both adjustments. More precisely, this analysis was done with 146 runs from pp collisions at $\sqrt{s} = 13$ TeV, corresponding to the time span 25th of September until the 26th of October.

After the preselection of the data set and the correlation parameters, some further restrictions were done to reduce the disturbance by potential outliers. The evaluation is done chamber by chamber and using the data from all runs for the respective chamber. In order for a data point of the corresponding run to contribute to the evaluation, the voltage settings for the gain and the drift velocity need to be above a certain threshold — 1450 V for the anode voltage and 1950 V for the drift voltage, corresponding to the lower edges of each voltage distribution — and the chamber needs to have a “good” status, i.e. was not marked as faulty during the data taking. For most of the chambers there are only few runs for which a data point does not fulfill the conditions, therefore sufficient statistics is reached to perform the analysis. However, there are some chambers having defective anode wires or the like, resulting in zero statistics. Those are excluded from analysis. Effectively, 436 chambers remain for the study. The selected data points are then further processed. Before the evaluation is described in all detail, the original conditions are specified. In Fig. 13 the development of the gain from the chosen data set over time and the projection to the y -axis are shown. Both plots depict the gain after the previously mentioned conditions were applied. The temporal development in the left-hand side plot yields rather strong fluctuations of the gain. Those short-term variations correspond to the fluctuating pressure and illustrate very well the need for an online pressure correction. By fitting the projection on the right-hand side with a Gaussian, the calculation of σ/μ yields a stability — i.e. the relative deviation to the nominal value, as a function of time — of the chamber gain of $(6.86 \pm 0.06)\%$, consistent with [12] (v_{drift} stability: $(1.15 \pm 0.01)\%$). Since the performance of the TRD trigger is strongly dependent on this stability — for an optimal performance a maximum stability of 1% of the gain is required —, the aim is to improve it. Observing the distribution further, one notices the tails on both edges. As well an indentation on top of the distribution can be seen. Those formations are caused by a structure of the gain over the detector (shown in App. A). The gain increases in each supermodule for middle stacks and decreases again for the outer ones. The reason for the occurrence of this structure is not yet known. As the indentation lies in the

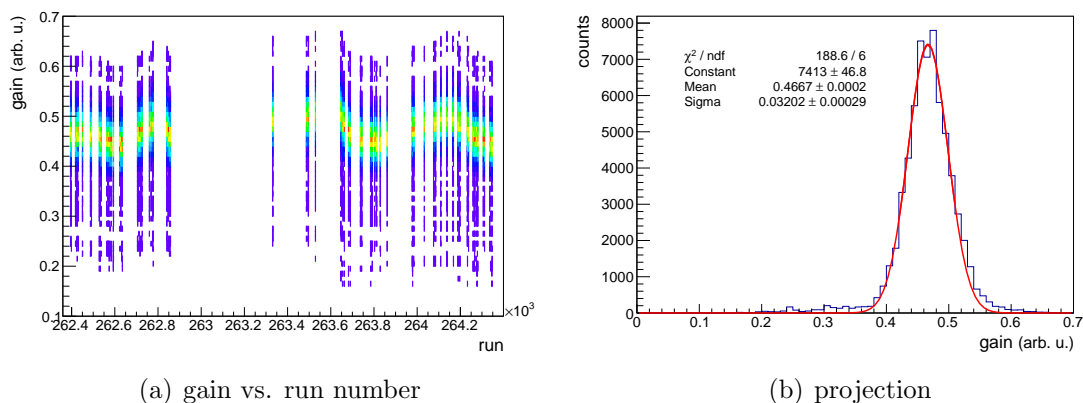


Figure 13: (a) Uncorrected gain vs run number and (b) projection to the y -axis. The run numbers indirectly represent the temporal development.

middle of the distribution, it could not be excluded from the analysis. Regarding the tails however, they were eliminated as far as possible, i.e. without decreasing the statistics significantly, by applying further cuts during the data selection. For the determination of the correlation, the gain had to be higher than 0.4 and lower than 0.52 (in arbitrary units) in order to contribute. As also described in the following sections, the correction is done by dividing the data points by the correlation function. Thus on the one hand the distributions for the gain and drift velocity are rescaled in this process, and on the other hand the tails are still present in the distributions used for the gas corrections. To eliminate the tails from the analysis also in this investigations, the cuts were done individually for every correction, adjusted to the respective distributions.

4.2 Pressure Correction

The strongest influencing factor to changes of the gain and drift velocity is the gas pressure. Therefore it is the parameter for which the correlation is determined first. As mentioned in the previous section the re-calibration of the gas chromatograph introduced a pressure dependence to the gas contents. This will be corrected for as well in Section 4.2.2.

4.2.1 Gain and Drift Velocity

First the pressure dependences of the gain and drift velocity were examined. All described steps apply to both the gain and drift velocity, in the following only the gain is mentioned explicitly.

To further ensure that outliers of the correlation gain vs pressure do not disturb the result, an averaging technique was used. The pressure was divided in bins, with the bin width determined by the accuracy at which the pressure can be measured by the pressure sensor. An exact number was not known, but [12] states a working pressure of 0.1 mbar above atmospheric pressure. Hence, the measurement precision is at least of this order, ideally even better. Assuming a decent accuracy of the mentioned number, a precision of 0.05 mbar was taken. For every pressure bin the weighted mean [25] of the gain was calculated. The weights are determined by the measurement uncertainties of the data points, calculated via the relative precision

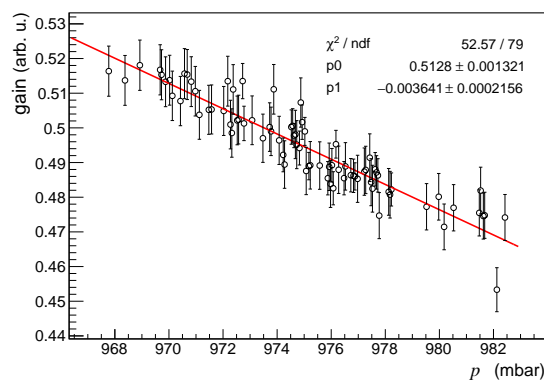


Figure 14: Gain - pressure correlation for chamber 77 after averaging the gain for each pressure bin using weights. A linear fit of the correlation was performed.

of 1.4 % (precision $v_{\text{drift}}=0.4\%$) [12]. An example for the averaged gain - pressure correlation for one chamber can be seen in Fig. 14.

In the next step, the correlation was fitted by a linear function. This function was displaced on the x -axis by 970 mbar, which is approximately the mean of the pressure distribution. The reason for this displacement is the otherwise strong correlation between the two parameters of the fit function, the slope and the intercept. The pressure values lie rather far away from the origin, which means that even a small change in the slope translates to a big change of the intercept. For a strong correlation of the fit parameters, the errors of the fit result are strongly dependent on small changes of slope and intercept [25]. The displacement avoids this and consequently the correlation between the parameters decreases. For the end result this does not change the dependence, i.e. the slope.

Next, the gain of the chamber is corrected for the pressure dependence. This is simply done by dividing the data points by the previously determined fit function, evaluated at the corresponding pressure value. The error of the pressure corrected value accordingly is calculated by Gaussian error propagation.

With the resulting correlation slopes also the adjustment parameters for the HV settings can be calculated. As mentioned before, the gain is already corrected online for pressure changes. For the data set used in this thesis the online correction was disabled. In this adjustment the high voltage of the anodes is corrected, using the relative slopes of the previously determined correlation. Hence

$$adj.parameter = \frac{\Delta g}{\Delta p} \cdot \frac{\bar{p}}{\bar{g}} \quad (9)$$

where $\frac{\Delta g}{\Delta p}$ is the slope from the pressure correlation and \bar{p} and \bar{g} are averaged pressure and averaged gain of the chamber, respectively. They are received by calling the function of the graph that returns the mean value of the desired axis via calculating the arithmetic mean of all values on the corresponding axis. The adjustment parameter for the drift voltage is calculated in the same manner. The determined HV adjustment parameter, i.e. the relative slope of pressure and gain, of each chamber is filled into a histogram. The distribution of adjustment parameters from all chambers can be seen in Fig. 15, for both the gain and drift velocity. The parameters

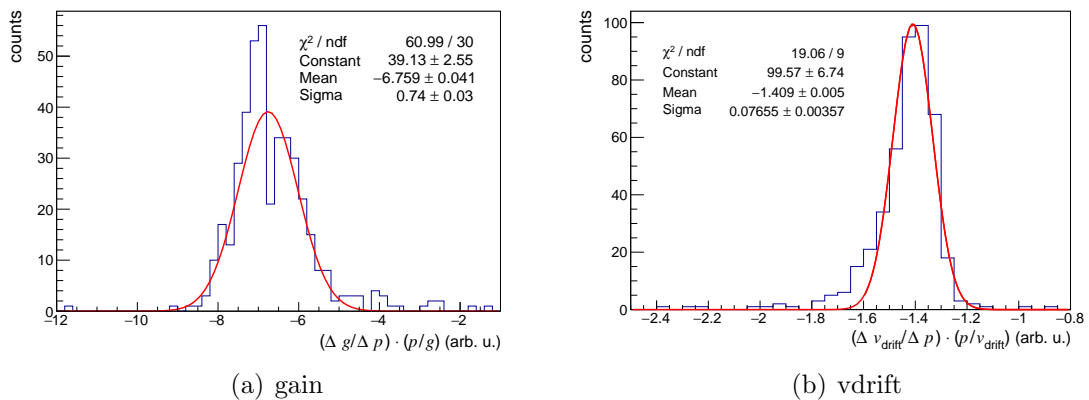


Figure 15: Adjustment parameters, i.e. relative slopes, from all chambers for the online pressure correction of (a) the gain and (b) the drift velocity.

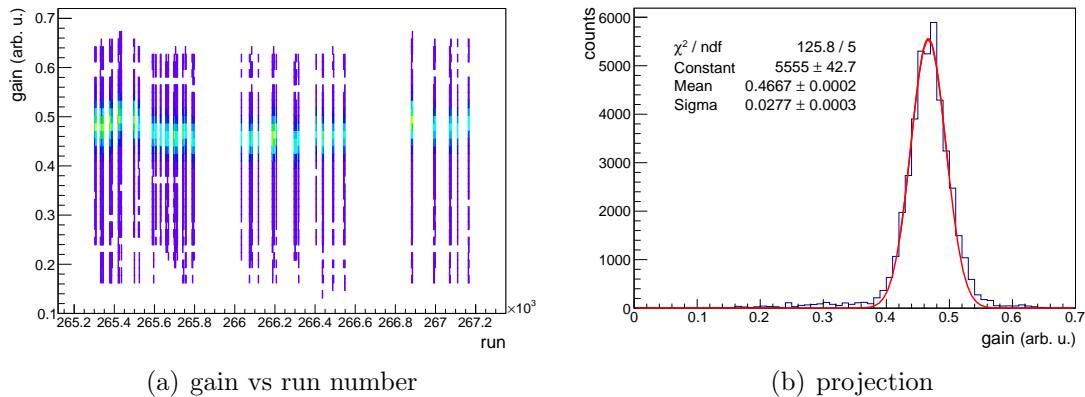


Figure 16: (a) Gain vs run number after the employment of the updated HV adjustment parameters. The two data sets with increased mean gain can be found around run numbers of 265 400 and 266 850. The run numbers indirectly represent the temporal development. (b) projection to the y -axis.

	Evaluation 2016	Final result
gain	-6.24 ± 0.05	-6.76 ± 0.04
v_{drift}	-1.40 ± 0.05	-1.409 ± 0.005

Table 2: HV adjustment parameters, i.e. relative slopes, from pressure correlation, determined by the mean of a Gaussian fit of the relative slopes from all chambers.

eventually employed in the online correction are the mean of the Gaussian fits on the distributions. As can be seen clearly in the left-hand side plot there is a gap at the center of the distribution for the relative slope of the gain. This originates from the previously observed indentation of the gain distribution in Fig. 13. For the calculation of the adjustment parameter the averaged gain of the corresponding chamber is used. As this averaged gain is not uniform for all chambers, the resulting parameter is located either on the left-hand side or the right-hand side of the gap, depending on whether the averaged gain is located more on the right-hand side or the left-hand side of the indentation. The gap could already be reduced by cutting the tails of the distribution, but since this indentation cannot be excluded, the gap cannot be eliminated completely. It was explained in Section 3.2 that the anode voltage is adjusted individually for every chamber to align the gain. In order to eliminate the gap in the distribution of adjustment parameters, this individual adjustment of the anode voltages needs to be optimised. The tail in the distribution for the adjustment parameter of the drift voltage for pressure corrections in Fig. 15(b) similarly originates from tails in the distribution of the uncorrected drift velocity.

The HV adjustment parameters have been calculated in a previous approach, using the same data set. Those parameters, as well as the results from this thesis are listed in Tab. 2. The differences of both parameters are mostly due to the changed averaging technique, which especially the gain was observed to be more sensitive to. The parameters of the analysis in 2016 have already been employed successfully in the TRD trigger period in p-Pb runs with $\sqrt{s_{NN}} = 5 \text{ TeV}$ and 8 TeV at the end of 2016, see Fig. 16. Shown there is the temporal development of the gain. Apart from two isolated run sets in between (run numbers between 265 410 and 265 450 for the first set and 266 880 to 266 890 for the second), the gain of the TRD showed a quite

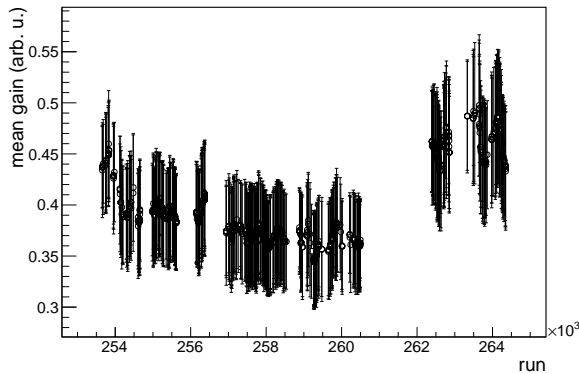


Figure 17: Mean gain vs run number. The mean gain is the averaged gain of all chambers, weighted with cathode pad response functions. The uncertainties are the resulting error from averaging. The run numbers, indirectly representing temporal development, show data from the year 2016.

constant behaviour. The two isolated sets are characterised by a sudden increase of the gain. It was tried to find out what caused this, but no explanation could be found up to now. After all, the gain returned to the nominal value in both cases. Excluding the runs with increased gain and projecting the remaining data to the y -axis, one again obtains the gain distribution. By fitting the distribution with a Gaussian and calculating the stability (width divided by mean), the pressure correction with the new parameters resulted in an improved stability of $(5.94 \pm 0.06) \%$. The mean gain, that is the averaged gain of all chambers, weighted with cathode pad response functions (the uncertainties are the resulting error from averaging), has a stability of 3.4% in the data set that was used for studies of this thesis. After the employment of the new parameters this stability improved to 3.1% . Also the stability of the drift velocity improved, in this case to 0.98% .

Applying a pressure correction certainly redounds to a better stability, yet further improvements can be achieved. For this purpose the dependence on the gas mixture was investigated in the following.

4.2.2 Gas contents

Looking at the mean gain and its development over the year 2016 (Fig. 17), one can see a continuous decrease, apart from the increase towards the end corresponding to the HV adjustment in August/September. Since the pressure changes in time spans of days but more or less stays in the same range for time spans of weeks or months, the overall decrease originates from the continuous increase of the N_2 contamination. This observation confirms the previous assumption of N_2 being a crucial factor.

Before the actual gas corrections of the gain and drift velocity can be performed, the mentioned pressure dependence of the single gas components, artificially introduced by the gas chromatograph, has to be corrected for as well. The correlation for N_2 is shown in Fig. 18. Similar to the previous pressure corrections of the gain and drift velocity, the single gas contents were averaged for every pressure bin. The uncertainty, with which the gas chromatograph measures the gas composition is not a relative but an absolute value [19]. Thus, as the uncertainty is the same for every data point, not the weighted average but the simple arithmetic mean was used in this case. The uncertainties are 0.023% , 0.026% and 0.018% for N_2 , Xe and CO_2 ,

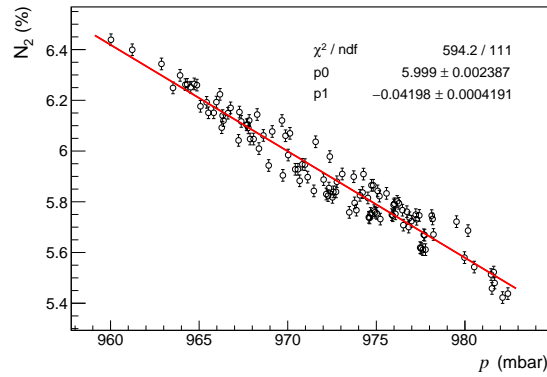


Figure 18: N₂ - pressure correlation. The error bars represent the measurement uncertainty of the gas chromatograph. A linear fit was performed

respectively. The correlation is, despite the fact that all gas contents were averaged, still quite broad. This can be explained by the fact, that the pressure fluctuates always in the same range around atmospheric pressure, whilst the increasing N₂ contamination steadily replaces and changes the contents of the other gas components, so they are continuously increasing or decreasing. Therefore, for one occurring pressure value, there are several different amounts of the gas components present in the detector. In the same way as the gain and drift velocity were corrected for their pressure dependences, the gas contents are corrected via division by the respective fit functions.

4.3 N₂ Correction

As explained in sections 2.2 and 3.2, the influence of N₂ on the drift velocity is assumed to be negligible. Therefore only the gain is addressed in this section.

4.3.1 Gain

In procedure similar to the pressure correction discussed in Section 4.2, the pressure corrected chamber gain was correlated with the pressure corrected N₂ content. The averaging technique was applied here as well. The bin width for binning N₂ was defined by the maximum uncertainty of 0.001 of the pressure corrected N₂. This was determined by extracting the upper edge of the corresponding uncertainty distribution. Again the gain was averaged for every N₂ bin, weighted with the errors of each data point introduced by the pressure correction. An exemplary correlation for a single chamber is shown in Fig. 19. Since both correlated quantities were divided by their corresponding fit functions, they are scaled to unity. When utilising the determined correlation slope, the “1” on each axis can be set to any desired value, e.g. the nominal gain and the ideal condition of 0% for N₂.

In the next step, the gain - N₂ correlation was fitted with a linear function, that was — as in the case for pressure — displaced by “1” in x direction in order to minimize the correlation between slope and intercept. Once again, the gain was divided by the correlation function and stored for further analysis.

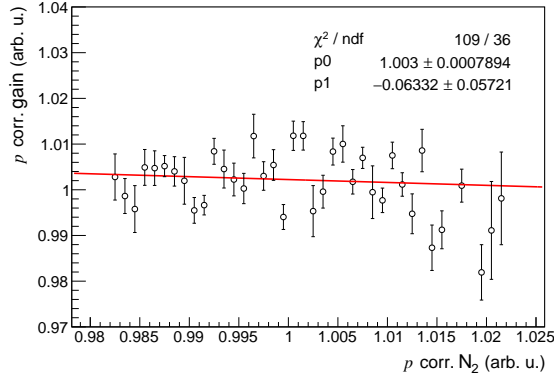


Figure 19: Gain - N_2 correlation for chamber 77 with pressure corrected gain and pressure corrected N_2 .

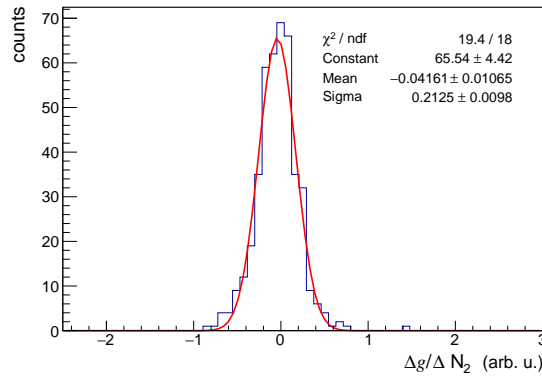


Figure 20: Slopes from the gain - N_2 correlations from all chambers.

The correlation slopes from all chambers can be seen in Fig. 20. Applying a Gaussian fit one can extract a mean slope of (-0.042 ± 0.011) . Considering now the rescaling of x and y axis, this translates to

$$\text{gain}(N_2) = \text{gain} \cdot [1 - (4.2 \pm 1.1)\% / \Delta N_2] \quad (10)$$

So the result of the correlation evaluation basically indicates that the gain decreases by 4.2% for each percent N_2 added. From Fig. 6 in Section 2.3, in order to keep the gain constant, the need for a HV adjustment of 50 V for every 10% N_2 added was extracted. Using results from the krypton (Kr) calibration, the gain increases by 0.8% when the voltage is increased by 1 V [26]. This translates to a decrease of the gain of 40% for 10% additional N_2 , which is in good agreement, with respect to the uncertainty, with the measured result.

4.3.2 Gas mixture

To be able to correct the gain for the ratio of CO_2 to Xe, a further dependence has to be considered. As the N_2 enters the detector volume through leaks, it gradually replaces the original gas mixture. Therefore the amounts of CO_2 and Xe, especially the ratio of both quantities, depend on the amount of N_2 , which is illustrated in Fig. 21 and explained in more detail in Section 5.1. The correlation is rising in an approximately linear way. There are some outliers, yet they have a larger uncertainty.

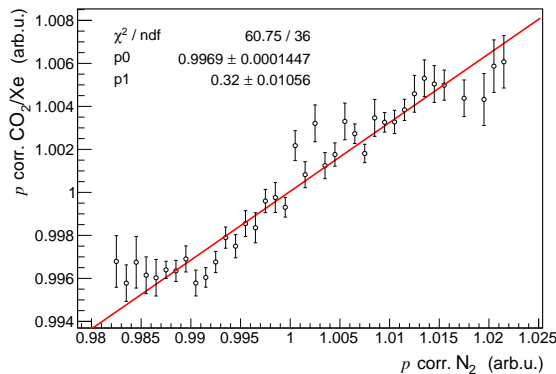


Figure 21: Correlation of the pressure corrected ratio of CO₂/Xe and the pressure corrected N₂.

Therefore the linear approach is assumed to be consistent with the measurements. The gain just had been corrected for any influences from N₂, so the ratio has to be corrected as well to enable an evaluation that is completely independent of the N₂ content. This is done in the same way as the other corrections before, by correlating the pressure corrected ratio with the pressure corrected N₂, fitting with a linear function and dividing the data points by this fit function.

4.4 CO₂/Xe Correction

In the last step of the evaluation, both the gain and drift velocity were corrected for the ratio of CO₂ and Xe, which ideally should be constant. However, as explained previously (Section 4.3.2), it changes over time due to the N₂ contamination. In case of the gain the N₂ corrected quantities were used. As the drift velocity has only been corrected for the pressure and not for the N₂ contamination, the only pressure corrected ratio was used in this case.

As before for the pressure and N₂ correction, the ratio was divided into bins — the bin width was again defined by the maximum uncertainty of the corrected ratio, 0.001 for the N₂ corrected ratio and 0.0015 for the pressure corrected one — and the weighted mean calculated for every bin. Example plots for both correlations are shown in Fig. 22. In both cases a correlation can be observed. For the drift velocity this is clearly linear. For the gain, the variation is very small (1 %) in comparison to comparison to Fig. 14 (10 %). Therefore, as for the other correlations before, a linear fit was performed. Again, the slopes from the gain-ratio correlation and the drift velocity-ratio correlation from all chambers were filled into histograms that can be seen in Fig. 23. For this correlation, the means of the Gaussian fits indicate the relative change of the gain or drift velocity for a relative change of the ratio.

$$\text{gain}(\text{CO}_2/\text{Xe}) = \text{gain} \cdot [1 - (0.41 \pm 0.03)/\Delta(\text{CO}_2/\text{Xe})] \quad (11)$$

$$v_{\text{drift}}(\text{CO}_2/\text{Xe}) = v_{\text{drift}} \cdot [1 - (0.461 \pm 0.005)/\Delta(\text{CO}_2/\text{Xe})] \quad (12)$$

For example will an increase of the CO₂ content by 1 %, when assuming N₂ is not part of the gas mixture, increase the ratio of CO₂ and Xe by 0.014. Applying this to the previous findings the gain decreases by (0.57 ± 0.04) % and the drift velocity

decreases by $(0.645 \pm 0.007)\%$. The drift velocity is therefore more dependent on the ratio of CO_2 and Xe than the gain. For the gain, the dependence on the amount of N_2 is clearly larger.

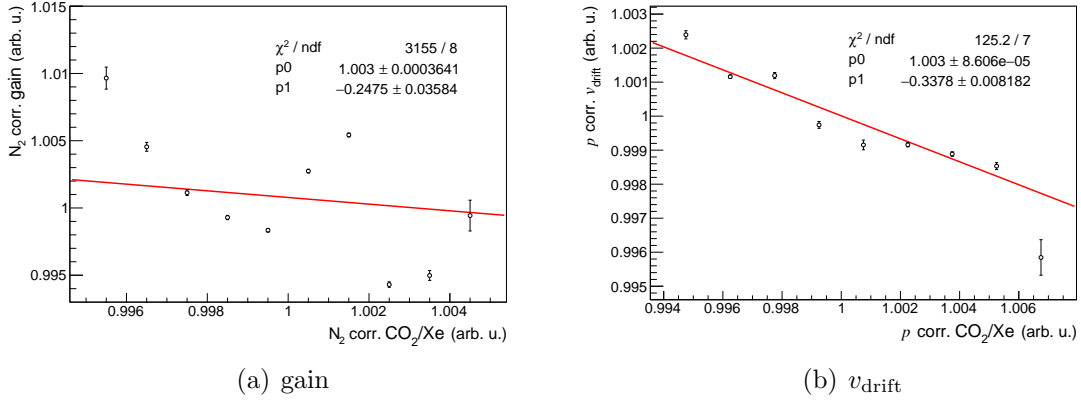


Figure 22: (a) Correlation of the pressure and N_2 corrected gain and ratio CO_2/Xe . (b) Correlation of the pressure corrected drift velocity and ratio CO_2/Xe . Both correlations are from chamber 77.

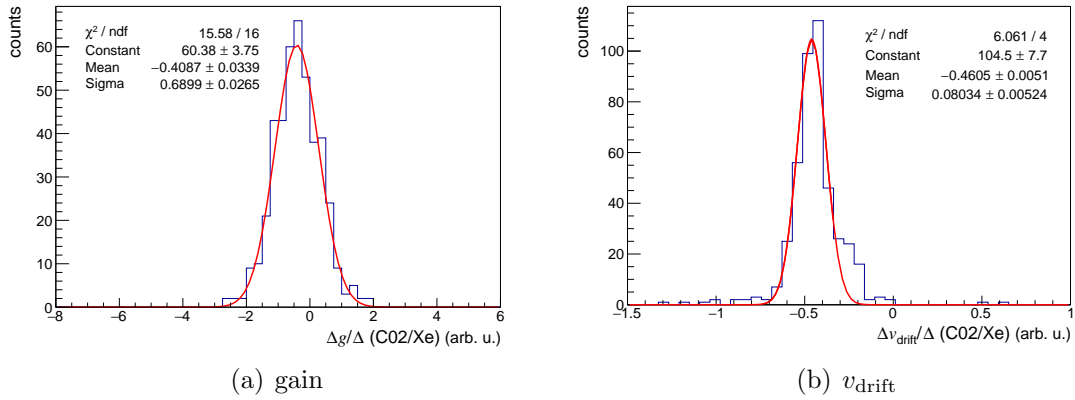


Figure 23: (a) Slopes from the gain - CO_2/Xe correlations from all chambers. (b) Slopes from the drift velocity - CO_2/Xe correlations from all chambers.

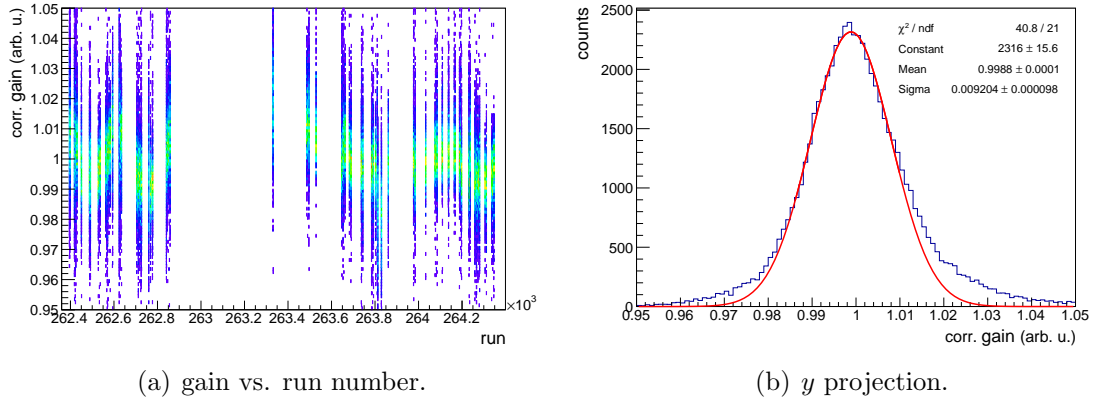


Figure 24: (a) Gain from all chambers after all corrections, as function of run number and (b) projection to the y -axis. The run numbers indirectly represent the temporal development.

	no correction	pressure corr.	N ₂ corr.	CO ₂ /Xe corr.
gain	$(6.86 \pm 0.06) \%$	$(1.034 \pm 0.001) \%$	$(0.94 \pm 0.01) \%$	$(0.92 \pm 0.09) \%$
v_{drift}	$(1.15 \pm 0.01) \%$	$(0.339 \pm 0.009) \%$	–	$(0.245 \pm 0.002) \%$

Table 3: Stability of gain and v_{drift} before all corrections and after the single corrections.

4.5 Gain and Drift Velocity after all Corrections

Similar to the raw gain in Section 4.1, the gain can be displayed as a function of time after all corrections have been applied (in the analysis code). This time dependent data, as well as the projection to the y -axis is shown in Fig. 24. The fluctuations of the gain are clearly reduced. The tails, which can be seen on both sides of the distribution, are the ones that also show in the original distribution (Fig. 13). Since they were only cut off for the determination of the correlation slopes, but not in the actual correction, they still show in this plot. The stabilities of the gain and drift velocity, calculated by dividing the width of the distribution by its mean, after every correction are summarised in Tab. 3. It becomes clear that by correcting both quantities for the mentioned dependences, a tremendous improvement in stability can be achieved.

The pressure correction was already employed successfully in the p–Pb/Pb–p runs in 2016. However, for an optimal performance of the TRD trigger a gain stability of 1% is required. Although a good improvement can already be achieved by correcting for pressure changes, the desired stability will only be reached by further correcting for changes of the gas mixture. As the dependence of the gain on N₂ is rather strong, a frequent adjustment of the anode voltage using the results from Section 4.3.1 is recommended. To balance the decrease of the gain due to the increasing N₂ contamination, the HV should be adjusted for every 1% N₂ that impurifies the detector. The dependence on CO₂/Xe is much weaker, nonetheless will the performance of the TRD be further improved when also a correction for this quantity is applied. Therefore an adjustment of the HV for a change of the ratio by 0.025 — i.e. a decrease of both the gain and drift velocity by about 1% — is recommended. To compare the outcome of the analysis, the correlations to the gas mixture are next compared to simulations.

5 Simulations of Gain and Drift Velocity

In this chapter the measurements of the previous section are compared to simulations, which are done using the Garfield programme [13]. The aim is to confirm the correlations found in the analysis and gather a detailed insight of the process of the gas contamination.

Garfield simulates the geometry of detector chambers and calculates electric and magnetic fields for a given geometry in a rather realistic way. Furthermore it can be employed to simulate the drift of electrons and ions and induced signals on the chamber wires. Originally only implemented for 2D chambers, the versions 3 and higher are able to handle 3D structures as well. The configuration files for Garfield are organized in cell sections, each representing one of the different parts of the simulation. The chamber layout, i.e. the position of wires, plates, etc., as well as voltage settings, is entered first in the `&CELL` section. A magnetic field can be defined in the `&MAGNETIC` cell, `&FIELD` can be used to plot and inspect the electric field that is generated by the voltage settings and arrangement of the wires. The transport properties of the gas the chamber is filled with are entered in the `&GAS` cell. This can be done either by applying measured values or by using Magboltz simulations [27].

The Magboltz simulation programme solves the Boltzmann transport equation for a given gas mixture, electric and magnetic field by performing Monte Carlo integrations under the inclusion of inelastic collision cross sections. For Magboltz versions up to 7, a Garfield interface is implemented and can therefore be called inside the program. However, on the one hand the calculations for all field strengths present in the detector — which typically range from 100 V/cm up to 500 000 V/cm — take, depending on the accuracy, several hours. So generating the gas data while executing the Garfield code for e.g. a signal calculation is highly impractical. On the other hand the parameters for the calculations, e.g. cross sections or excitation and ionisation levels of the gases, are constantly updated and improved. Therefore it is advisable to take the most recent version available and run it standalone. Magboltz can handle gas mixtures of up to six gases that can be chosen from currently 50 components. Furthermore information on gas pressure and temperature have to be provided in the input file. When all needed input is supplied, Magboltz computes different transport properties like drift velocity (Section 2.2), attachment and diffusion coefficients, but also the Townsend coefficient and production rates for all ionisation and excitation levels of the single gas components. The latter can be used to correct the Townsend coefficient for the Penning transfer (Section 2.3). The resulting parameters, i.e. the drift velocity, penning corrected Townsend coefficient, attachment coefficients etc., can then be inserted in Garfield in the form of tables and used in the following calculations.

When the gas mixture with all its properties is defined, the simulated detector chamber can be used to investigate the behaviour of electrons and ions in it. For this purpose the cells `&DRIFT` and `&SIGNAL` are available. While `&SIGNAL` can be used for the purpose its name indicates — namely defining the track of a traversing particle along which ionisation clusters are build and computing the resulting signal on the chosen wire(s) — the `&DRIFT` cell is a bit more versatile. Like in the `&SIGNAL` cell, one possibility is to define a track and drift the resulting ionisation particles from there on. The other possibility is to select a certain point anywhere in the chamber from which a particle, i.e. an electron, positron or positive or negative ion,

drifts along the field lines. Garfield has several commands to access the informations of this motion, among them drift time, diffusion, attachment or multiplication.

5.1 Simulating the TRD

In the following, the approach to simulate a realistic TRD readout chamber with the aim of computing its gain and drift velocity for different gas mixtures is described. As explained previously, the simulation consists of two stages. Before extracting the gas gain and drift velocity from Garfield, the transport properties for different gas mixtures were computed using Magboltz version 11.2. For the different calculations, the default values for pressure and temperature, i.e. 760 Torr and 20 °C, were taken. To investigate the influence of the N₂ contamination on the gain and drift velocity independent from the ratio of CO₂ and Xe, the amounts of the first data set were chosen such that CO₂/Xe was kept constant, based on the nominal mixture of Xe-CO₂ [85-15], i.e. a ratio of ³/17. The N₂ content was increased from 0 % to 10 % in steps of 2 %.

Next, the gas mixtures for the comparisons to the results from Section 4 were generated. In this case as well, admixtures of N₂ from 0 % to 10 % in the same iteration steps, were simulated. There are two possibilities for what can happen to the original gas when the N₂ enters. The first that comes to mind is the even replacement of both Xe and CO₂, i.e. for 2 % N₂ there are 1 % less in amount of each of the other gases (Xe-CO₂ [85-5] → Xe-CO₂-N₂ [84-14-2]). So when the 10 % of N₂ are reached, there are 80 % Xe and 10 % CO₂ remaining in the detector. Although this seems logical, it does not really describe reality. If the process was like this, the ratio of CO₂ and Xe decreased for an increasing N₂ amount. However, as can be seen in Section 4.3, the ratio increases with increasing contamination. The reason for this can be found in the source of the N₂. It contaminates the detector gas as it enters as a component of the surrounding air. Apart from N₂ and the filtered out O₂ and H₂O, see Section 3.3.3, also CO₂ is an integral part of this mixture. As CO₂ is as well part of the intended detector gas mixture, it is not filtered out. Therefore together with the N₂ contamination the CO₂ content increases and results in an increasing ratio of CO₂ to Xe. Unfortunately, the exact amount of CO₂ being added is not known. On account of this an estimate had to be made. In comparison, N₂ has a much higher percentage in air than CO₂. Therefore the addition of CO₂ is much smaller than that of N₂, the exact amount depending on the air quality in the LHC tunnel. For this thesis it was assumed that the increase of CO₂ is 10 % of the increase in N₂, i.e. +0.2 % CO₂ in every iteration step. The Xe amount has been adjusted such that the amounts of all components add up to 100 %. To validate the considerations, gas characteristics for both described scenarios have been simulated. For the calculation of the gain and drift velocity, all gas mixtures were simulated for field strengths from 100 V/cm to 500 000 V/cm. An exemplary input file, as well as an example of the extracted gas tables can be seen in App. B. As stated before, the Townsend coefficients still require a correction for the Penning transfer. The highest excitation level of Xe is insufficient to ionise CO₂. However, CO₂ has several excited states with energies higher than the ionisation energy of Xe (12.13 eV), hence the Penning transfer occurs from CO₂ to Xe. The correction is done by employing [28]

$$\alpha_{\text{Pen}} := \alpha \left(1 + r_{\text{Pen}} \frac{f^{\text{exc}}}{f^{\text{ion}}} \right), \quad (13)$$

with f^{exc} and f^{ion} being the sum of excitation rates of CO_2 and the ionisation rate of Xe, respectively. Those are extracted from the Magboltz output. Basically, CO_2 has around 100 excited states in this output. However, for most of them the probability for the CO_2 atoms being in those states is considerably low and they are therefore neglected. In the calculation only the two levels closest to the ionisation energy are included in the sum for f^{exc} . The Penning fraction r_{Pen} is taken from [20], in being 24 % for mixtures with no N_2 added and 22 % for mixtures containing N_2 . When all gas files have been generated, the calculation of the gain and drift velocity can be performed. For this reason, first the TRD geometry [19] was defined. It consists of two cathode planes, one set to ground potential and the other one set to the nominal drift voltage of -2150 V . Furthermore two rows of wires are implemented, one row of cathode wires — as well on ground potential — and one row of anode wires, set to the nominal voltage of 1520 V . The planes and wires are arranged as in Fig. 9, Section 3.2. The gas tables consist of discrete entries for the electric field and the corresponding gas properties. The drift velocity is computed by Garfield by extrapolating the entries of the entered gas tables for the electric field strength defined by the voltage settings. For the gain calculations, several electrons were drifted from the drift region to the anode wires. They were all started at the same distance to the anode wires, but the starting position parallel to the anode wire plane was iterated from left to right in steps of 0.0002 cm . At the boundaries of the chosen drift area, the electrons drifted outside this area. To ensure that the test particles all stay inside the area, the range of starting points was limited. This resulted in a reduction of the total number of iterations from 5000 — chosen to achieve sufficient statistics — to 4325. In the amplification area an avalanche is formed and the multiplication can be accessed by calling the corresponding variable in the drift function. For every gas mixture the multiplication factors of all 4325 independent calculations are filled into a histogram and fitted by a Gaussian function. The mean of this fit represents the actual gas gain.

Before the results are presented, considerations about the reliability should be made. The main uncertainty on the performance is introduced by the uncertainties of the gas mixture. The gas tables with the transport properties do not contain the uncertainty of the variables, i.e. they are assumed to be exact. However, as mentioned before, the parameters in Magboltz are updated constantly. This already indicates that the knowledge of this parameters is by means not accurate, thus by excluding the uncertainty of the transport properties the uncertainty of the resulting gain is underestimated. In addition, a not yet solved issue [29] with the Magboltz program prevented a continuous execution of the gas simulation, as the program ceased from operating for more than two electric field strengths in a row, beginning at 4000 V/cm . As a consequence, the simulations had to be done in steps. However, as has been noted in the investigations, the outcome of the computation was dependent on whether the calculation for the current field strength was preceded by another one or if it was started with the current one. The results in both cases differed slightly. The order of magnitude of the error that is introduced by this issue cannot be estimated effectively, but it should be kept in mind. Furthermore, the accuracy is limited by the value of NMAX, the number of real collisions that are simulated to obtain the gas properties. The higher this number is chosen the higher is the accuracy but also the computation time. For practical reasons, NMAX was set to 3 — in multiples of 10^7 — which results in an accuracy of about 1 % of the gas properties.

5.2 Results

The simulated gas gain and drift velocity as functions of the different gas mixtures are shown in Fig. 25 and Fig. 26, respectively. In the left figures, the dependence for an increasing N_2 content is shown, for the three different scenarios containing N_2 , i.e. the first, where CO_2 and Xe were replaced evenly by N_2 , the second in which the ratio of CO_2 and Xe was kept constant and the third with additional CO_2 for every addition of N_2 . More differential studies for the gain and drift velocity from the simulations can be found in App. B. For the gain it is apparent that it decreases with increasing N_2 contamination for all scenarios. The set with the least decline is the blue one, where the CO_2 and Xe contents are replaced in even amounts by N_2 . The dependence is

$$\Delta g = -2.24\%/\Delta N_2.$$

So for an even replacement the gain decreases by -2.24% for every 1% N_2 added. The uncertainties for this and the following dependences are on the order of magnitude of 10^{-4} and therefore negligible. As explained in Section 5.1, the uncertainties are expected to be underestimated, which is confirmed by the simulation results. The green points, representing the set where the ratio of CO_2 and Xe was kept constant, have a steeper dependence of

$$\Delta g = -2.81\%/\Delta N_2.$$

In both cases, the CO_2 content decreases with increasing N_2 contamination. As can be seen in the plot on the right-hand side of Fig. 25, the gas gain is higher for less CO_2 , in particular the gain increases by 1.08% for each percent of CO_2 less in the gas mixture. As the CO_2 content decreases faster in the former of both data sets, where CO_2 and Xe are replaced evenly, the dependence of the gain on changes of the N_2 content is lower there. The model of an even replacement was also employed by S. Dyba [30] in simulations of the dependences of the gain on the gas mixture. In [30], a decrease of $(3.00 \pm 0.21)\%$ per added percent of N_2 was found. With respect to the uncertainties, this is in good agreement with the correlation found in this thesis.

The third set, in red, represents the attempt of simulating a realistic N_2 contamination, i.e. the CO_2 content — and thus the ratio — increases together with the N_2 content. The dependence of the gain on the amount of N_2 ,

$$\Delta g = -3.42\%/\Delta N_2,$$

is here the strongest among the simulated scenarios. It is also the one that has, with respect to the uncertainties, the best agreement to the measured results shown in Section 4.3, where a slope of $(-4.2 \pm 1.1)\%$ was obtained.

As mentioned previously the simulations yield for the dependence of the gain on the ratio of CO_2 to Xe a decrease of 1.08% for every 1% CO_2 added. The correlation found in the measurements was a decrease of the gain by $(0.57 \pm 0.04)\%$ for an increase of 1% in the amount of CO_2 , which is lower than the correlation resulting from the simulations. To determine which of the both simulated results is more

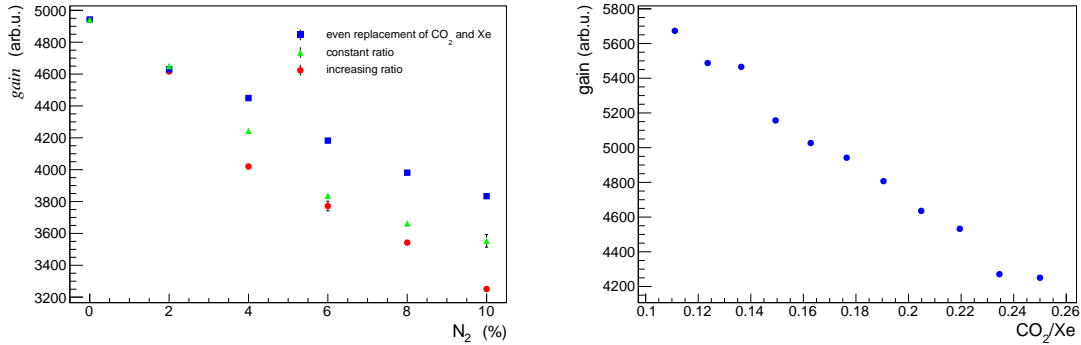


Figure 25: Left: Simulated gain as a function of the N₂ content, for different scenarios on the replacement of the original gas mixture (blue: 2% N₂ replace 1% of CO₂ and Xe each; green: CO₂/Xe is constant; red: +0.2% CO₂ for each 2% N₂ added). Right: Simulated gain as a function of the ratio of CO₂ to Xe, no admixtures of N₂.

realistic, a third value for the correlation was consulted. [30] found in simulations a relative change of the gain of $(-1.20 \pm 0.02)\%$ for a relative change of the CO₂ content of 1%. This is even higher than the result of the simulations of this thesis and not consistent with these experimental findings within the uncertainties, therefore no definitive conclusion can be made. To identify the accurate value of the dependence more studies with larger statistics have to be performed.

However, for the relative dependence of the gain on the N₂ contamination, the previously made assumptions were confirmed. As expected, the set with increasing CO₂ and N₂ content is the best approach to describe the processes in the TRD. However, there is still room for further investigations. Although in good agreement with respect to the uncertainties, the relative dependence resulting from the simulations is still lower than the measured one. Hence, the chosen iterations of +0.2% CO₂ for 2% N₂ are not the ideal description. By increasing the added CO₂ amount, the best description of the data can be found. Moreover, as can be seen by the outliers in the right-hand side plot of Fig. 25, even higher statistics is preferable to improve the precision of the simulation. Furthermore, by choosing smaller steps for the N₂ increasement, one would gather a more detailed insight on this dependence, especially in the range of 2% to 4%. As can be seen in the left-hand side plot, for up to 2% N₂, the points of all three results are similar, while they are separated clearly for higher amounts. A finer stepsize will reveal the structure in between. It is also recommendable to repeat the simulations with Magboltz for all field strengths in one pass, as with the thereby improved accuracy of the gas properties it may be possible to correct outliers like the ones in the green set at 6% and 8% N₂ content. It should also be noted that the found agreement of measurement and data is only valid regarding relative dependences. The absolute values for the gain do not coincide with the measurements. However, by adjusting the simulations in the described way, an agreement of measurement and data will be achieved in future for the absolute values as well.

The results of the simulations of the drift velocity are shown in Fig. 26. The colour code in the plots is the same as for the gain. As can be seen in the green set, where the only influence for a change of the drift velocity is the change of the N₂ content, no significant dependence is observable. Therefore the reason that the drift velocity is decreasing with increasing N₂ content in the red set — the scenario

which was confirmed to be the most realistic one in the gain studies — is the simultaneous increase of the CO_2 content and the therefore increasing ratio of CO_2 to Xe. This observation confirms the considerations of Section 2.2 and validates the approach of Section 4. The blue set implies an increasing behaviour of the drift velocity with increasing N_2 contamination, as the CO_2 content, and thereby the ratio, decreases simultaneously. This reinforces even more that an even replacement of the original gas mixture is not a realistic approach. The plot on the right-hand side shows the dependence of the simulated drift velocity on the ratio and reveals not a linear but a rather exponential correlation. As the range of the gas contents is much smaller in the measurement data than in the simulated data set, the linear approach of Section 4.4 is justified, but it makes a comparison of numbers difficult. However, in Section 4.4 a decrease of $(0.645 \pm 0.005) \%$ was measured. Averaging the relative decreases between the single steps of the simulated data set, a mean decrease of 6.46 % was observed, which is larger than the measured result by an order of magnitude. As in the case of the gain, a larger data set and more studies are necessary to obtain clarification about the accurate value of the dependence of the drift velocity on the ratio of CO_2 to Xe.

However, all in all the simulations were already quite successful in showing the expected trends for all the studied correlations and a very good agreement of the measured and simulated relative correlation between the gain and the N_2 contamination was found.

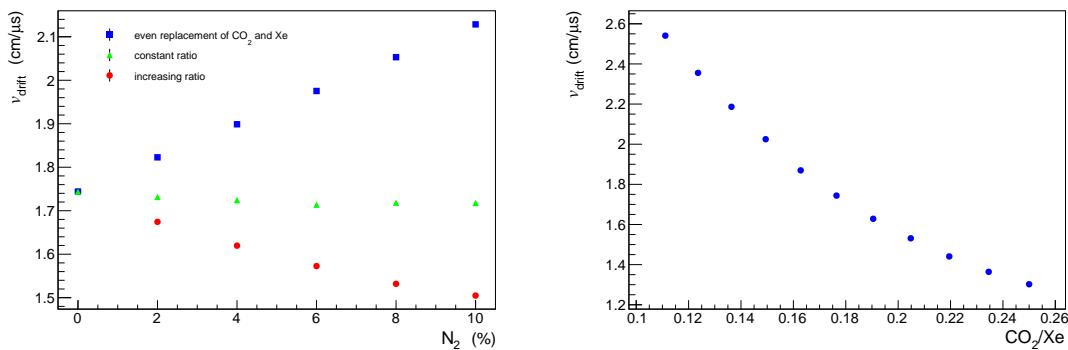


Figure 26: Left: Simulated drift velocity as a function of the N_2 content, for different scenarios on the replacement of the original gas mixture (blue: 2 % N_2 replace 1 % of CO_2 and Xe each; green: CO_2/Xe is constant; red: +0.2 % CO_2 for each 2 % N_2 added).

Right: Simulated drift velocity as a function of the ratio of CO_2 to Xe, no admixtures of N_2 .

6 Summary and Outlook

In this thesis the dependences of the gain and drift velocity of the readout chambers of the ALICE Transition Radiation Detector on properties like pressure and gas mixture were investigated. A study of those correlations is of particular interest, as the results can be used to correct both quantities online for occurring changes of the pressure and gas mixture. This is of high importance, as the gain in particular is required to be constant over time within 1% of the nominal value to achieve a sufficient performance of the TRD trigger. The findings were compared to simulations performed with the Magboltz and Garfield programs.

The correlations were investigated step by step, starting with the pressure. By determining the relative slope of both gain vs pressure and drift velocity vs pressure, new HV adjustment parameters for an online correction for pressure fluctuations were calculated. Additionally, the performance of preliminarily calculated parameters, using data from pp collisions 2016 at $\sqrt{s} = 13$ TeV, was evaluated. They were successfully employed in p-Pb collisions at $\sqrt{s_{NN}} = 5$ TeV and 8 TeV and improved the gain stability, i.e. the deviation of the gain relative to the nominal value, as a function of time, by 1%. In the analysis, both gain and drift velocity were corrected for their pressure dependence and then correlated with the gas mixture in the next step. The N₂ dependence was only studied for the gain, as findings in publication papers stated the dependence to be negligible for the drift velocity. As expected, a rather strong gain - N₂ correlation was found. For every 1% N₂ added, the gain decreased by (4.2 ± 1.1) %. In the last part of the data analysis the dependence on the ratio of CO₂ to Xe was investigated for both the gain and drift velocity. For the gain, this dependence was much smaller than the one on N₂.

All in all, a major improvement of the gain and drift velocity stability was achieved in the data analysis. Without any corrections, the gain in this data set holds a stability of 6.8%. After applying the corrections for all correlations to the data, a stability of (0.92 ± 0.01) % was obtained. This result is of particular value for the TRD, as it fulfills the aim of the gain being stable within 1%. An application of the correlation slopes in online corrections will improve the electron PID and thus triggering capability of the TRD tremendously. For the drift velocity, the uncorrected stability is 1.15%. By correcting the data points for the pressure correlation and the dependence on CO₂/Xe, the stability was improved to (0.245 ± 0.002) %.

In the second part of this thesis, the dependences of the gain and drift velocity on the gas mixture were studied by performing simulations. The gas mixture of the TRD and the resulting multiplication factor and drift velocity were simulated using the Magboltz and Garfield programs, respectively. As it is necessary to use the most recent version of both programs, the Magboltz interface in Garfield could not be used. The Magboltz version linked to Garfield uses outdated information about the gases, so its use would impair the accuracy of the gain and drift velocity calculations. Nonetheless, by running Magboltz standalone, the calculated gas properties were sufficiently accurate to compute reasonable gains and drift velocities. In comparison to the measured correlations the simulated data shows good agreement for the relative dependence of the gain on the N₂ contamination and confirm the overall trend seen in all correlations.

The analyses in this thesis showed that gain and drift velocity offer a wide range of possibilities for more differential studies. The comparison of the previous findings with resulting correlations from larger data sets improves the statistics and validates the results contained in this thesis. Regarding the simulations, a broader range of the gas compositions with finer incremental steps between them will improve our knowledge of the overall structure of the dependences. Furthermore, a more detailed study of the N₂ contamination, i.e. varying the amount of CO₂ that enters the detector together with the N₂, is desirable, as it helps to understand the underlying mechanisms of the contamination. When the exact process of gas replacement by contaminating air is found, the study can be extended to investigate the behaviour of the gain and drift velocity for the change of more than one parameter. The simultaneous variation of both pressure and gas composition in a multidimensional study will complete our understanding of the dependences of the gain and drift velocity on all the relevant parameters. By including also the minor influences of O₂, H₂O and the temperature, an accurate description can be achieved and be used to optimise the performance of the TRD and thereby the performance of ALICE.

A Data Analysis Plots

Plots from the data analysis, that were not shown in the main evaluation, are listed here.

A.1 Uncorrected Quantities

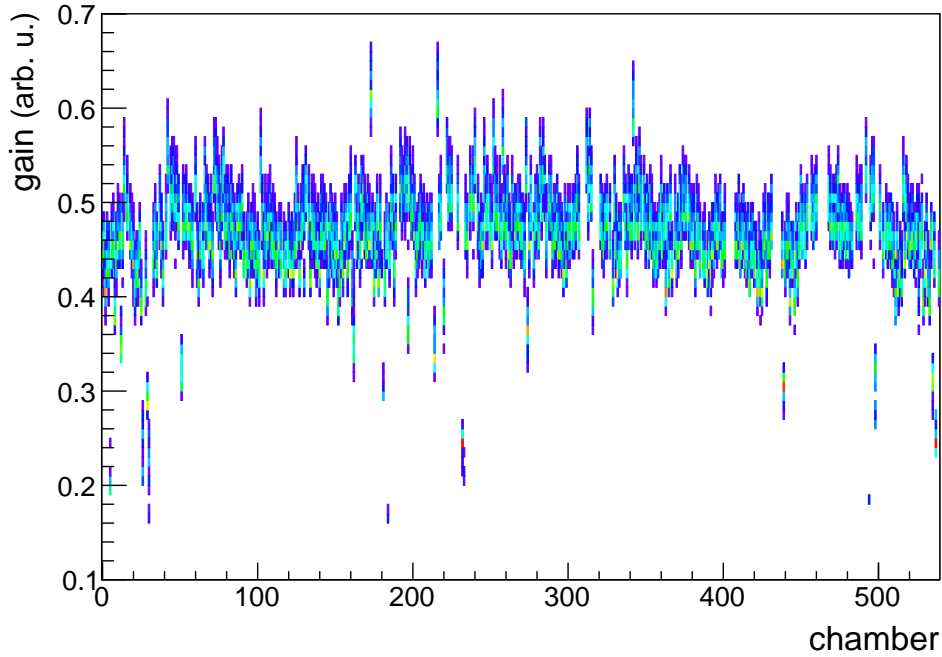


Figure 27: Uncorrected gain vs chamber number. The gain increases for chambers in middle stacks and decreases for outer stacks.

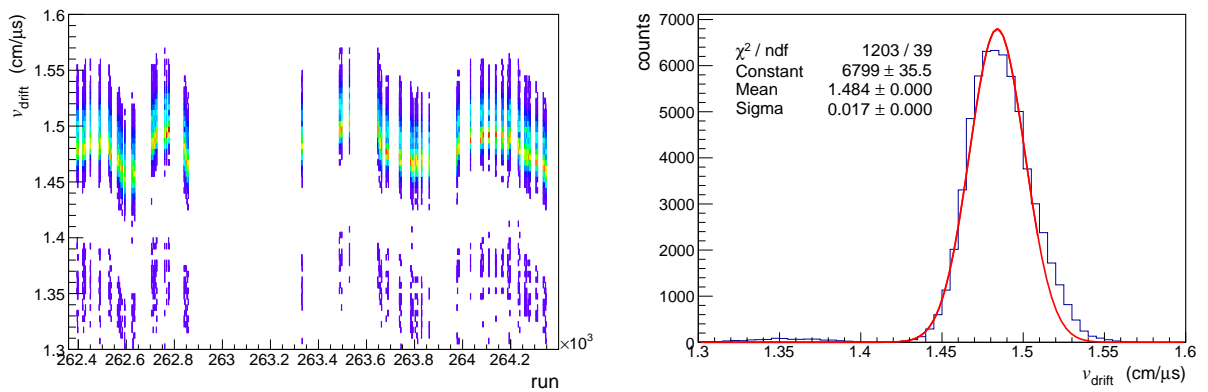


Figure 28: Left: Uncorrected drift velocity vs run number. Right: projection to the y -axis

A.2 Gain and Drift velocity after the single corrections

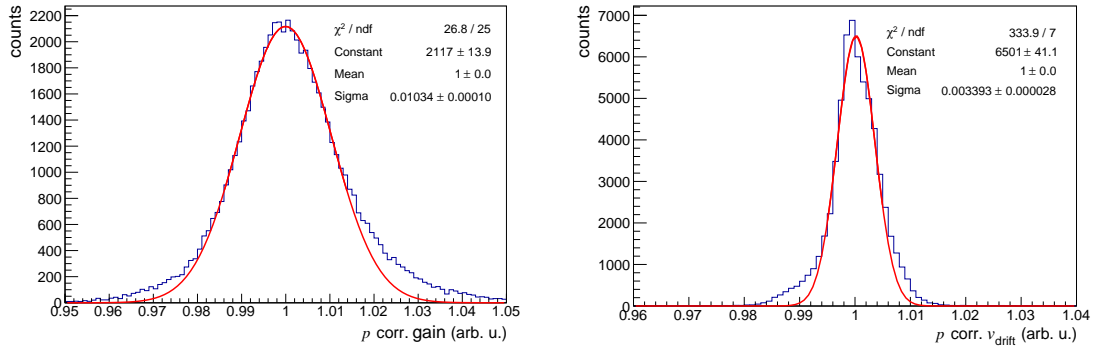


Figure 29: Gain and drift velocity after the correction for the pressure dependence.

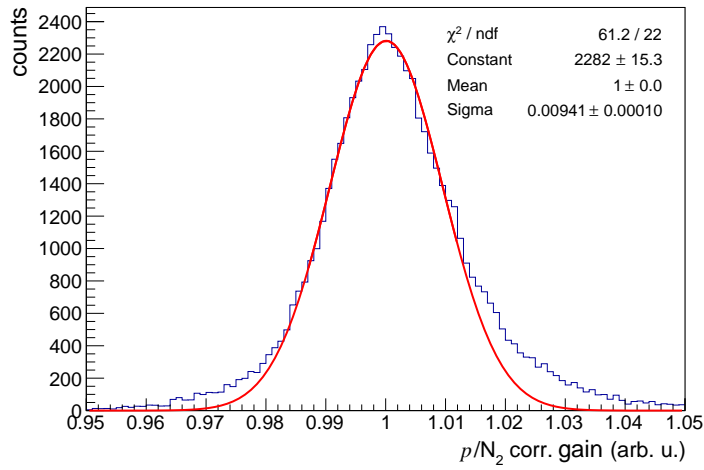


Figure 30: Gain after the correction for the N₂ dependence.

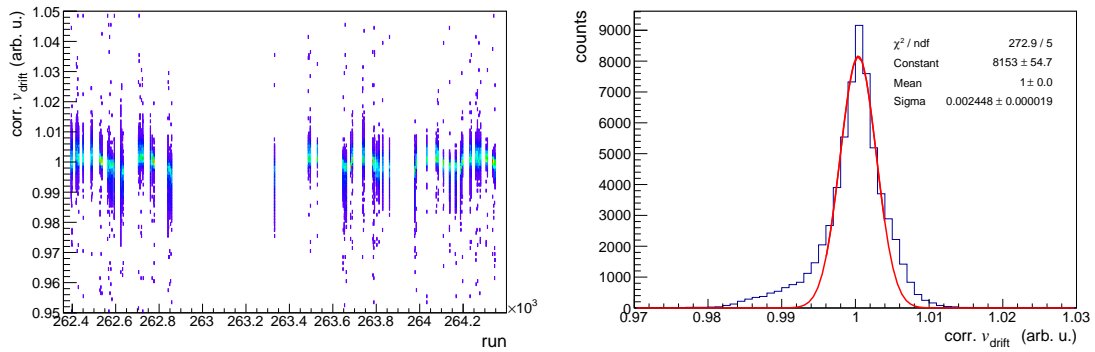


Figure 31: Left: drift velocity after all corrections vs run number. Right: projection to the y -axis. The tails correspond to the tails of the original distribution.

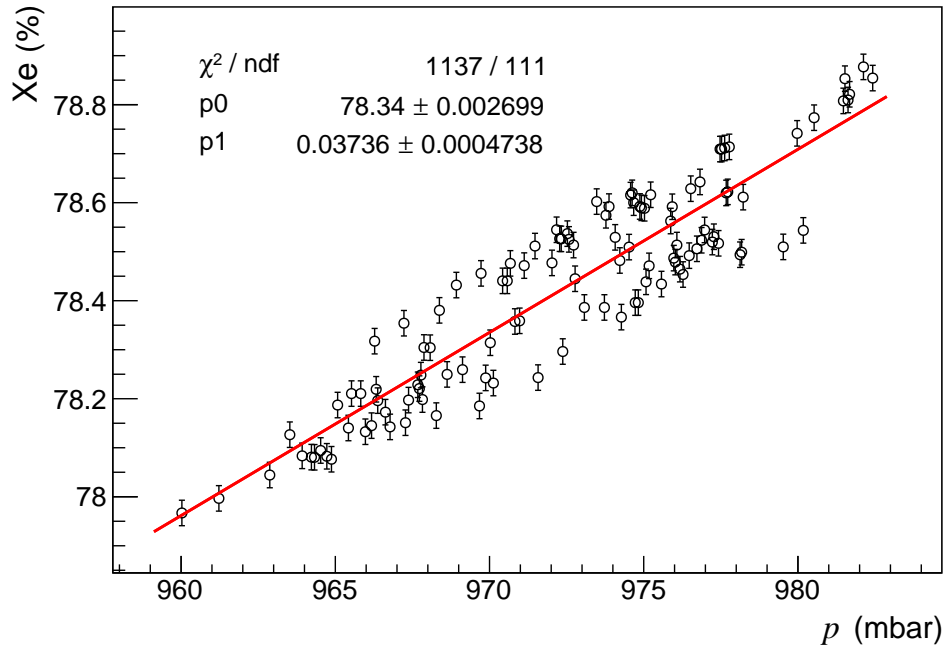
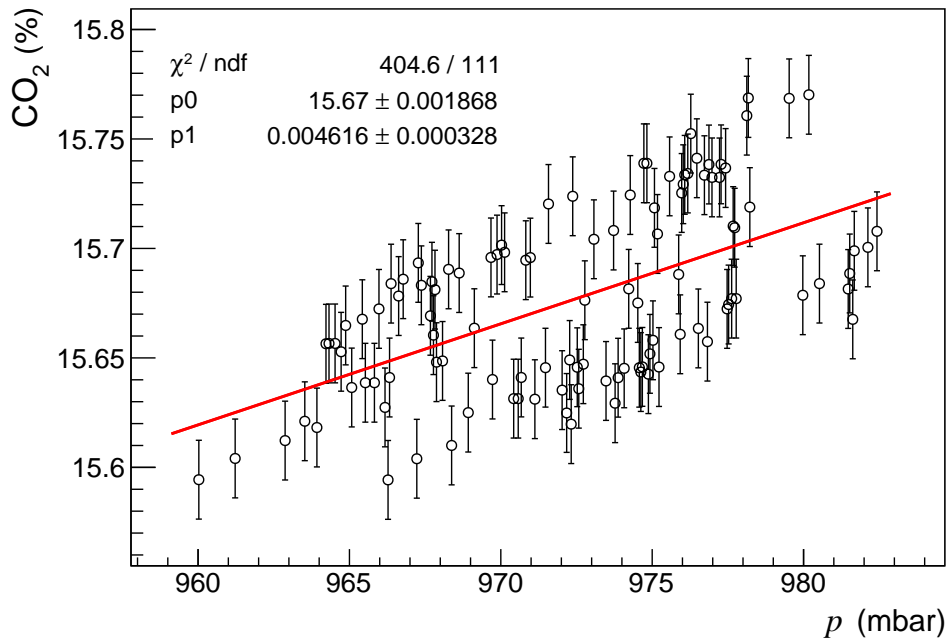
A.3 Pressure correlation of Xe and CO₂

Figure 32: Xe vs pressure.

Figure 33: CO₂ vs pressure.

B Simulation files

B.1 Generating files

```
      3      4      0      0      15.0
    7 12 16  0  0  0
  84.0    14.0    2.0    0.0    0.0    0.0    20.0
760.0
10000.0    0.0    0.0
      3      3      0      0      20.0
    7 12 16  0  0  0
  84.0    14.0    2.0    0.0    0.0    0.0    20.0
760.0
12000.0    0.0    0.0
      3      3      0      0      20.0
    7 12 16  0  0  0
  84.0    14.0    2.0    0.0    0.0    0.0    20.0
760.0
14000.0    0.0    0.0
      3      3      0      0      20.0
    7 12 16  0  0  0
  84.0    14.0    2.0    0.0    0.0    0.0    20.0
760.0
16000.0    0.0    0.0
      3      3      0      0      20.0
    7 12 16  0  0  0
  84.0    14.0    2.0    0.0    0.0    0.0    20.0
760.0
18000.0    0.0    0.0
      3      4      0      0      30.0
    7 12 16  0  0  0
  84.0    14.0    2.0    0.0    0.0    0.0    20.0
760.0
20000.0    0.0    0.0
```

Figure 34: Generating file for Magboltz. First line: number of gases, number of real collisions, command to calculate penning fraction, inclusion of thermal gas motion, upper limit of electron energy; Second line: gas indentifiers; third line: amounts of the single gases, temperature in celsius and pressure in Torr; fourth line: electric field, magnetic field and angle between them. [29]

```

****
** Cell definition
*****
%CELL

reset
opt layout

cell-id "TRD"

plane y=3.0 V=-2150.

plane y=-.7 V=0.

define vanode 1520.

*enter wires: name, #number, diameter, x, y, voltage
rows
k 10 .0075 .25*i 0. 0.
s 5 .0020 .125+.5*i -.35 vanode

period x=2.5
*****
****
**gas definition
*****
%GAS

IF (n2=0)
Then
< Xe85CO215_gas.txt

Endif

*****

*%MAIN

*global field=2150./3.

*global drift

*Call drift_velocity(field, drift)

*Say "drift velocity: {drift}"

*%QUIT

*****gain calculation
*****

&DRIFT
area 0. -0.8 1. 1.
**area -0.2 -1. 2.4 3.3
**area -1.3 -0.62 1. 3.02

integration-parameters integration-accuracy 1e-9 maximum-step-length 0.2

Call plot_drift_area

Call book_histogram(gain1,50,'autoscale')

**Call book_histogram(ion, 50, 0, 2500)

For i From 0 To NumbAval Do

**Call avalanche(0.6, 0.6, 0., 'plot-electron,plot-ion,townsend',ne,ni)

Call drift_electron_3(0.01+0.0002*i, 0.9, 0, status1, time1, diffusion1,
multil)

Call plot_drift_line

Call plot_end

Say "multiplication: {multil}, (avalanche {i})"

Call fill_histogram(gain1, multil)

Enddo

Call plot_end

**store histograms

Call list_histograms

Call write_histogram(gain1, HistFile)

**Call write_histogram(ion, HistFile)

*****
****
**fit histogram
*****

Call get_histogram(gain1, HistFile)

Call fit_gaussian(gain1, int, mean, sigma)

Say "Mean Gain: {mean} +- {sigma}"

*****

```

Figure 35: Garfield input file [19]

B.2 Gas table

```

table e/p townsend drift long-diff trans-diff attach-coeff
0.13158 0.00000 0.1287E+00 0.3562E+02 0.3595E+02 0.0000E+00
0.26316 0.00000 0.2690E+00 0.4067E+02 0.4392E+02 0.0000E+00
0.39474 0.00000 0.4234E+00 0.6009E+02 0.4818E+02 0.0000E+00
0.52632 0.00000 0.6081E+00 0.9214E+02 0.6025E+02 0.0000E+00
0.65789 0.00000 0.8426E+00 0.1576E+03 0.8650E+02 0.0000E+00
0.78947 0.00000 0.1153E+01 0.2521E+03 0.1254E+03 0.0000E+00
0.92105 0.00000 0.1546E+01 0.5191E+03 0.2067E+03 0.0000E+00
1.05263 0.00000 0.2008E+01 0.6562E+03 0.3638E+03 0.0000E+00
1.18421 0.00000 0.2497E+01 0.8068E+03 0.5382E+03 0.0000E+00
1.31579 0.00000 0.2959E+01 0.8981E+03 0.7062E+03 0.0000E+00
1.44737 0.00000 0.3391E+01 0.9237E+03 0.9120E+03 0.0000E+00
1.57895 0.00000 0.3735E+01 0.9129E+03 0.1046E+04 0.0000E+00
2.63158 0.00000 0.4657E+01 0.4764E+03 0.1828E+04 0.0000E+00
3.94737 0.00000 0.4763E+01 0.4064E+03 0.1742E+04 0.1702E-02
5.26316 0.00000 0.4840E+01 0.3621E+03 0.1788E+04 0.1026E-01
6.57895 0.00000 0.4887E+01 0.3530E+03 0.1703E+04 0.9894E-01
13.1579 0.00000 0.4862E+01 0.3412E+03 0.1335E+04 0.1387E+01
15.7895 0.00000 0.4901E+01 0.3633E+03 0.1180E+04 0.2486E+01
18.4211 0.00000 0.5020E+01 0.3827E+03 0.1304E+04 0.3057E+01
21.0526 0.00000 0.5214E+01 0.4629E+03 0.1111E+04 0.3357E+01
23.6842 0.00000 0.5449E+01 0.4951E+03 0.1010E+04 0.3645E+01
26.3158 38.8000 0.5739E+01 0.4573E+03 0.9746E+03 0.3840E+01
39.4737 176.000 0.7435E+01 0.6107E+03 0.9714E+03 0.3799E+01
52.6316 384.500 0.9337E+01 0.6338E+03 0.9368E+03 0.3292E+01
65.7895 631.200 0.1132E+02 0.6196E+03 0.9545E+03 0.2856E+01
131.579 2040.20 0.2182E+02 0.1013E+04 0.9659E+03 0.1450E+01
263.158 4833.20 0.4382E+02 0.1220E+04 0.1231E+04 0.6310E+00
657.895 10684.2 0.1086E+03 0.2761E+04 0.2548E+04 0.1216E+00

heed xenon 80.6 co2 15.4 n2 4.

Vector epmonte asst fion fexc longdiff transdiff attco
100.00000 0.0 1.0000E+00 0.0000E+00 0.3562E+02 0.3595E+02
0.0000E+00
200.00000 0.0 1.0000E+00 0.0000E+00 0.4067E+02 0.4392E+02
0.0000E+00
300.00000 0.0 1.0000E+00 0.0000E+00 0.6009E+02 0.4818E+02
0.0000E+00
400.00000 0.0 1.0000E+00 0.0000E+00 0.9214E+02 0.6025E+02
0.0000E+00
500.00000 0.0 1.0000E+00 0.0000E+00 0.1576E+03 0.8650E+02
0.0000E+00
600.00000 0.0 1.0000E+00 0.0000E+00 0.2521E+03 0.1254E+03
0.0000E+00
700.00000 0.0 1.0000E+00 0.0000E+00 0.5191E+03 0.2067E+03
0.0000E+00
800.00000 0.0 1.0000E+00 0.0000E+00 0.6562E+03 0.3638E+03
0.0000E+00
900.00000 0.0 1.0000E+00 0.0000E+00 0.8068E+03 0.5382E+03
0.0000E+00
1000.0000 0.0 1.0000E+00 0.0000E+00 0.8981E+03 0.7062E+03
0.0000E+00
1100.0000 0.0 1.0000E+00 0.0000E+00 0.9237E+03 0.9120E+03
0.0000E+00
1200.0000 0.0 1.0000E+00 0.0000E+00 0.9129E+03 0.1046E+04
0.0000E+00
2000.0000 0.0 1.0000E+00 0.0000E+00 0.4764E+03 0.1828E+04
0.0000E+00
3000.0000 0.0 1.0000E+00 0.0000E+00 0.4064E+03 0.1742E+04
0.1702E-02
4000.0000 0.0 1.0000E+00 0.0000E+00 0.3621E+03 0.1788E+04
0.1026E-01
5000.0000 0.0 1.0000E+00 0.0000E+00 0.3530E+03 0.1703E+04
0.9894E-01
10000.000 0.0 1.0000E+00 0.0000E+00 0.3412E+03 0.1335E+04
0.1387E+01
12000.000 0.0 1.0000E+00 0.0000E+00 0.3633E+03 0.1180E+04
0.2486E+01
0.2486E+01

14000.000 0.0 1.0000E+00 0.0000E+00 0.3827E+03 0.1304E+04
0.3057E+01
16000.000 0.0 1.0000E+00 0.0000E+00 0.4629E+03 0.1111E+04
0.3357E+01
18000.000 0.0 1.0000E+00 0.0000E+00 0.4951E+03 0.1010E+04
0.3645E+01
20000.000 38.8 0.2252E-03 0.0000E+00 0.4573E+03 0.9746E+03
0.3840E+01
30000.000 176.0 0.1364E-02 0.7616E-07 0.6107E+03 0.9714E+03
0.3799E+01
40000.000 384.5 0.3818E-02 0.1207E-05 0.6338E+03 0.9368E+03
0.3292E+01
50000.000 631.2 0.7834E-02 0.5245E-05 0.6196E+03 0.9545E+03
0.2856E+01
100000.00 2040.2 0.5131E-01 0.1667E-03 0.1013E+04 0.9659E+03
0.1450E+01
200000.00 4833.2 0.2444E+00 0.2119E-02 0.1220E+04 0.1231E+04
0.6310E+00
500000.00 10684.2 0.1201E+01 0.2625E-01 0.2761E+04 0.2548E+04
0.1216E+00

global frac .22

global p=760
pressure (p) Torr
temperature 20 celsius
global epmonte=epmonte/p
global asst=asst/p
global asst=asst*(fion+fexc*frac)/fion
global longdiff=longdiff*sqrt(p)
global transdiff=transdiff*sqrt(p)
global attco=attco/sqrt(p)
replace townsend asst vs epmonte
replace long-diff longdiff vs epmonte
replace trans-diff transdiff vs epmonte
replace attach-coeff attco vs epmonte

```

Figure 36: Gas table. First block: results from Magboltz; Second block: same data including ionisation and excitation frequencies; Third block: Penning correction and adjustment of transport properties to reduced electric field.

B.3 Results of the simulations

In the following, the results from the Garfield simulations are listed. The values for the correlations, given in the main evaluation, were determined by calculating the change of all single steps between the results for the different gas compositions and averaging over them. This was done for every data set individually. The values for the gain are the means of the individual Gaussian fits of the distributions from all 4325 independent calculations, performed by Garfield. The programme did not return an uncertainty for the drift velocity.

CO ₂ (%)	Xe (%)	gain (arb. u.)	vdrift
10.0	90.0	5672.71 ± 1.37	2.54082
11.0	89.0	5487.49 ± 1.31	2.35545
12.0	88.0	5465.45 ± 1.33	2.18637
13.0	87.0	5156.80 ± 1.24	2.02489
14.0	86.0	5026.74 ± 1.10	1.86974
15.0	85.0	4942.08 ± 0.97	1.74394
16.0	84.0	4807.00 ± 0.94	1.62842
17.0	83.0	4635.84 ± 1.03	1.53113
18.0	82.0	4532.54 ± 0.98	1.44085
19.0	81.0	4271.09 ± 0.87	1.36416
20.0	80.0	4250.64 ± 1.01	1.30224

Table 4: Gas mixture with no N₂ added.

N ₂ (%)	CO ₂ (%)	Xe (%)	gain (arb. u.)	vdrift
0.0	15.0	85.0	4942.08 ± 0.97	1.74394
2.0	15.2	82.8	4616.39 ± 0.97	1.67438
4.0	15.4	80.6	4020.05 ± 0.90	1.61968
6.0	15.6	78.4	3771.76 ± 30.2	1.57274
8.0	15.8	76.2	3542.14 ± 0.66	1.53190
10.0	16.0	74.0	3251.00 ± 0.68	1.50492

Table 5: Increasing ratio of CO₂ to Xe.

N_2 (%)	CO_2 (%)	Xe (%)	gain (arb. u.)	vdrift
0.0	15.0	85.0	4942.08 ± 0.97	1.74394
2.0	14.0	84.0	4630.13 ± 1.12	1.82274
4.0	13.0	83.0	4449.40 ± 1.05	1.89879
6.0	12.0	82.0	4182.53 ± 0.91	1.97534
8.0	11.0	81.0	3981.07 ± 0.76	2.05309
10.0	10.0	80.0	3833.75 ± 0.79	2.12855

Table 6: Even replacement of CO_2 and Xe by N_2 .

N_2 (%)	CO_2 (%)	Xe (%)	gain (arb. u.)	vdrift
0.0	15.0	85.0	4942.08 ± 0.97	1.74394
2.0	14.7	83.3	4650.67 ± 1.15	1.73177
4.0	14.4	81.6	4243.93 ± 0.89	1.72448
6.0	14.1	79.9	3836.62 ± 0.49	1.71386
8.0	13.8	78.2	3662.64 ± 0.67	1.71845
10.0	13.5	76.5	3553.06 ± 39.4	1.71799

Table 7: Constant ratio of CO_2 to Xe.

References

- [1] M. Thomson, *Modern particle physics*. Cambridge University Press, Cambridge, 2013.
- [2] P. Braun-Munzinger and J. Stachel, “The quest for the quark-gluon plasma,” *Nature* **448** (2007) 302–309.
- [3] L. Yan, P. Zhuang, and N. Xu, “ J/ψ Production in Quark-Gluon Plasma,” *Phys. Rev. Lett.* **97** (2006) 232301.
- [4] **ALICE** Collaboration, P. Cortese *et al.*, *ALICE Technical Design Report of the Transition Radiation Detector*. Technical Design Report ALICE. CERN, Geneva, 2001. <https://cds.cern.ch/record/519145>.
- [5] L. Evans and P. Bryant, “LHC Machine,” *JINST* **3** (2008) S08001.
- [6] ATLAS web page, January, 2017. <http://atlas.cern/>.
- [7] CMS web page, January, 2017. <http://cms.web.cern.ch/>.
- [8] **ATLAS** Collaboration, G. Aad *et al.*, “Observation of a new particle in the search for the Standard Model Higgs boson with the ATLAS detector at the LHC,” *Physics Letters B* **716** (2012) 1–29.
- [9] **CMS** Collaboration, S. Chatrchyan *et al.*, “Observation of a new boson at a mass of 125 GeV with the CMS experiment at the LHC,” *Physics Letters B* **716** (2012) 30–61.
- [10] LHCb web page, January, 2017. <https://lhcb.web.cern.ch/lhcb/>.
- [11] **ALICE** Collaboration, K. Aadmomt *et al.*, “The ALICE experiment at the CERN LHC,” *JINST* **3** (2008) S08002.
- [12] **ALICE** Collaboration, “The ALICE Transition Radiation Detector: construction, operation and performance,”. to be submitted.
- [13] R. Veenhof. <http://garfield.web.cern.ch/garfield/>.
- [14] **Particle Data Group** Collaboration *Chin. Phys. C* **37** . <http://pdg.lbl.gov/>.
- [15] V. L. Ginzburg and I. M. Frank, “Radiation of a uniformly moving electron due to its transition from one medium into another,” *J. Phys.(USSR)* **9** (1945) 353–362. [*Zh. Eksp. Teor. Fiz.*16,15(1946)].
- [16] B. Dolgoshein, “Transition radiation detectors,” *Nucl. Instrum. Meth.* **A326** (1993) 434 – 469.
- [17] W. R. Leo, *Techniques for Nuclear and Particle Physics Experiments*. Springer, Berlin ; Heidelberg, 2., rev. ed., 1994.
- [18] W. Blum, W. Riegler, and L. Rolandi, *Particle Detection with Drift Chambers*. Particle Acceleration and Detection. Springer, Berlin ; Heidelberg, 2. ed., 2008.

- [19] C. Garabatos: private communication.
- [20] A. Andronic, S. Biagi, P. Braun-Munzinger, C. Garabatos, and G. Tsileidakis, “Drift velocity and gain in argon- and xenon-based mixtures,” *Nucl. Instrum. Meth.* **A523** (2004) 302 – 308.
- [21] A. Zastawny, “Standardization of gas amplification description in proportional counters,” *Nucl. Instrum. Meth.* **A385** (1997) 239 – 242.
- [22] M. Fleck, “Commissioning a gas chromatograph for automatic measurements of gas compositions in the ALICE TPC and TRD and measurement of electrons from semi-leptonic heavy-flavour hadron decays in p-Pb collisions at $\sqrt{s_{NN}}=5.02$ TeV with the ALICE TRD,” Master Thesis, Ruprecht-Karls-Universität Heidelberg, 2014.
- [23] B. A. Heß, “Online Electron Identification for Triggering with the ALICE Transition Radiation Detector,” Diploma Thesis, Ruprecht-Karls-Universität Heidelberg, 2011.
- [24] Y. Pachmayer: private communication.
- [25] G. Bohm and G. Zech, *Introduction to statistics and data analysis for physicists*. Deutsches Elektronen-Synchrotron, Hamburg, 2010.
- [26] J. H. Stiller, “Gain Calibration of the ALICE TRD using the Decay of ^{83m}Kr and Alignment of the ALICE TRD,” Diploma Thesis, Ruprecht-Karls-Universität Heidelberg, 2011.
- [27] S. Biagi, “A multiterm Boltzmann analysis of drift velocity, diffusion, gain and magnetic-field effects in argon-methane-water-vapour mixtures,” *Nucl. Instrum. Meth.* **A283** (1989) 716.
<http://magboltz.web.cern.ch/magboltz/>.
- [28] O. Sahin, T. Z. Kowalski, and R. Veenhof, “High-precision gas gain and energy transfer measurements in Ar-CO₂ mixtures,” *Nucl. Instrum. Meth.* **A768** (2014) 104 – 111.
- [29] R. Veenhof: private communication.
- [30] S. Dyba, “Simulationen zur Gasverstärkung im ALICE-TRD und im Driftmonitor GOOFIE,” Diploma Thesis, Westfälische Wilhelms-Universität Münster, 2012.

Acknowledgements

First of all, I would like to thank Johanna Stachel for giving me the opportunity to work in this group during my thesis. It offered a great insight into this interesting field.

I would also like to thank Klaus Reygers for reading and evaluating my bachelor thesis.

Many thanks go to Yvonne Pachmayer for her support, expertise and constant encouragement during these past months. She was always available, even on weekends, to provide both great advice and motivation.

Furthermore I would like to express my gratitude to Rob Veenhof, Chilo Garabatos and Mesut Arslanok for their support with Magboltz and Garfield and for providing input files for both programmes.

Thanks also to Yvonne Pachmayer, Alice Ohlson, Sebastian Klewin and Hans Beck for proofreading this thesis, even at (very) short notice.

Thanks go to everybody from the ALICE group in Heideberg. I really enjoyed being part of this group, the discussions in the meetings and all those non work-related activities. Special thanks go to Hannah Klungenmeyer for the conversations during some much needed tea breaks.

Last but not least I want to thank my parents for their great support and love during my studies and the work on this thesis.

Erklärung

Ich versichere, dass ich diese Arbeit selbstständig verfasst und keine anderen als die angegebenen Quellen und Hilfsmittel benutzt habe.

Heidelberg, den 27.03.2017,